



# JGR Solid Earth

## RESEARCH ARTICLE

10.1029/2022JB025745

### Key Points:

- North American absolute P-wavespeed tomographic model incorporating dense seismic networks in Canada and Alaska
- Imaged fast wavespeed subducted remnants suggest revision of Alaskan and proto Pacific subduction models is necessary
- Slow wavespeed structures imply Slave Craton metasomatic modification and tectonic inheritance during Cordilleran orogenesis

### Supporting Information:

Supporting Information may be found in the online version of this article.

### Correspondence to:

A. Boyce,  
alistair.boyce@univ-lyon1.fr

### Citation:

Boyce, A., Liddell, M. V., Pugh, S., Brown, J., McMurchie, E., Parsons, A., et al. (2023). A new P-wave tomographic model (CAP22) for North America: Implications for the subduction and cratonic metasomatic modification history of western Canada and Alaska. *Journal of Geophysical Research: Solid Earth*, 128, e2022JB025745. <https://doi.org/10.1029/2022JB025745>

Received 6 OCT 2022

Accepted 23 FEB 2023

### Author Contributions:

**Conceptualization:** A. Boyce, M. V. Liddell, I. D. Bastow  
**Data curation:** A. Boyce, M. V. Liddell, S. Pugh, J. Brown, E. McMurchie, A. Parsons, C. Estève, S. Burdick, F. A. Darbyshire, A. J. Schaeffer, P. Audet, D. L. Schutt, R. C. Aster  
**Formal analysis:** A. Boyce, M. V. Liddell, S. Pugh, J. Brown, E. McMurchie, A. Parsons, F. A. Darbyshire

© 2023. The Authors.

This is an open access article under the terms of the [Creative Commons Attribution License](#), which permits use, distribution and reproduction in any medium, provided the original work is properly cited.

## A New P-Wave Tomographic Model (CAP22) for North America: Implications for the Subduction and Cratonic Metasomatic Modification History of Western Canada and Alaska

A. Boyce<sup>1,2</sup> , M. V. Liddell<sup>3</sup>, S. Pugh<sup>1</sup> , J. Brown<sup>1</sup>, E. McMurchie<sup>1</sup>, A. Parsons<sup>1</sup>, C. Estève<sup>4</sup>, S. Burdick<sup>5</sup>, F. A. Darbyshire<sup>3</sup> , S. Cottaar<sup>1</sup> , I. D. Bastow<sup>6</sup> , A. J. Schaeffer<sup>7</sup> , P. Audet<sup>8</sup> , D. L. Schutt<sup>9</sup> , and R. C. Aster<sup>9</sup>

<sup>1</sup>Department of Earth Science, Bullard Laboratories, University of Cambridge, Cambridge, UK, <sup>2</sup>Now at Université Claude Bernard Lyon 1, ENS de Lyon, CNRS, UMR 5276 LGL-TPE, Villeurbanne, France, <sup>3</sup>Centre de recherche Geotop, Université du Québec à Montréal, Montréal, QC, Canada, <sup>4</sup>Department of Meteorology and Geophysics, University of Vienna, Vienna, Austria, <sup>5</sup>Geology Department, Wayne State University, Detroit, MI, USA, <sup>6</sup>Department of Earth Science and Engineering, Royal School of Mines, Prince Consort Road, Imperial College London, London, UK, <sup>7</sup>Geological Survey of Canada Pacific Division, Sidney, BC, Canada, <sup>8</sup>Department of Earth and Environmental Sciences, University of Ottawa, Ottawa, ON, Canada, <sup>9</sup>Department of Geosciences and Warner College of Natural Resources, Colorado State University, Fort Collins, CO, USA

**Abstract** Our understanding of the present-day state and evolution of the Canadian and Alaskan mantle is hindered by a lack of absolute P-wavespeed constraints that provide complementary sensitivity to composition in conjunction with existing S-wavespeed models. Consequently, cratonic modification, orogenic history of western North America and complexities within the Alaskan Proto-Pacific subduction system remain enigmatic. One challenge concerns the difficulties in extracting absolute arrival-time measurements from often-noisy data recorded by temporary seismograph networks required to fill gaps in continental and global databases. Using the Absolute Arrival-time Recovery Method (AARM), we extract >180,000 new absolute arrival-time residuals from seismograph stations across Canada and Alaska and combine these data with USArray and global arrival-time data from the contiguous US and Alaska. We develop a new absolute P-wavespeed tomographic model, CAP22, spanning North America that significantly improves resolution in Canada and Alaska over previous models. Slow wavespeeds below the Canadian Cordillera sharply abut fast wavespeeds of the continental interior at the Rocky Mountain Trench in southwest Canada. Slow wavespeeds below the Mackenzie Mountains continue farther inland in northwest Canada, indicating Proterozoic-Archean metasomatism of the Slave craton. Inherited tectonic lineaments colocated with this north-south wavespeed boundary suggest that both the crust and mantle may control Cordilleran orogenic processes. In Alaska, fast upper mantle wavespeeds below the Wrangell Volcanic Field favor a conventional subduction related mechanism for volcanism. Finally, seismic evidence for the subducted Kula and Yukon slabs indicate tectonic reconstructions of western North America may require revision.

**Plain Language Summary** Our understanding of the plate tectonic history of North America is incomplete. Outstanding questions include: 1. Have ancient parts of the North American plate been modified over time or remained unchanged since assembly? 2. What processes produced the differing shape of the western Canadian Cordilleran Mountains along their length? 3. Can we image the old plate remnants that were recycled back into the mantle at subduction zones to better understand how North America was formed? We use earthquakes that produce P-waves, recorded at distant receivers, to seismically image the mantle below North America, including new data from Canada and Alaska for the first time. Slower-than-expected seismic wavespeeds that continue from the west coast inland toward north-central Canada suggest the ancient Slave Craton has been modified by chemical processes  $\geq$ 500 million years ago. An abrupt seismic wavespeed boundary perpendicular to the Canadian Cordilleran Mountains suggests their shape may be controlled by pre-existing zones of weakness in the crust and mantle. Fragments of old tectonic plates, stuck in the mantle below western North America and Alaska, suggest our understanding of the final stages of assembly of modern North America requires revision.

**Funding acquisition:** A. Boyce, M. V. Liddell, F. A. Darbyshire, S. Cottaar, I. D. Bastow, D. L. Schutt, R. C. Aster

**Investigation:** A. Boyce, J. Brown, E. McMurchie, A. Parsons

**Methodology:** A. Boyce, M. V. Liddell, S. Pugh, C. Estève, S. Burdick, F. A. Darbyshire, I. D. Bastow

**Project Administration:** A. Boyce, M. V. Liddell, I. D. Bastow

**Resources:** S. Burdick, S. Cottaar, I. D. Bastow

**Software:** A. Boyce, S. Burdick

**Supervision:** A. Boyce, S. Pugh, F. A. Darbyshire, S. Cottaar, I. D. Bastow

**Validation:** A. Boyce, P. Audet

**Visualization:** A. Boyce

**Writing – original draft:** A. Boyce

**Writing – review & editing:** A. Boyce, M. V. Liddell, S. Pugh, C. Estève, S. Burdick, F. A. Darbyshire, S. Cottaar, I. D. Bastow, A. J. Schaeffer, P. Audet, D. L. Schutt, R. C. Aster

## 1. Introduction

### 1.1. Overview

P-wave wavespeed tomographic models (e.g., Burdick et al., 2017; Schmandt & Lin, 2014) can offer higher lateral resolution than their S-wave counterparts (e.g., Darbyshire et al., 2013; Schaeffer & Lebedev, 2014); they also offer complementary sensitivity to temperature and composition (Schutt & Lesser, 2006), providing a valuable diagnostic tool for the causes of mantle seismic heterogeneity. However, their utility for addressing tectonic questions is often limited by overlying seismic station distribution.

In North America, deployment of the USArray Transportable Array (TA) seismic network across the contiguous United States has produced numerous new tectonic insights using seismic tomography (e.g., Schaeffer & Lebedev, 2014; Schmandt & Lin, 2014). However, the termination of the USArray deployment at or near the US-Canadian border, across which many significant geological boundaries traverse (Figure 1), has by comparison, largely limited seismological insights into the Canadian mantle to regional studies using temporary seismic networks (e.g., Mercier et al., 2009; Frederiksen et al., 2013; Bao et al., 2014; Boyce et al., 2016; Liddell et al., 2018; Y. Chen et al., 2019; Estève et al., 2019, 2020).

One successful attempt to combat the issue of tomographic resolution decay north of the USArray TA experiment incorporated absolute arrival-time measurements from temporary seismograph stations in southeast Canada into a continental scale P-wavespeed model including USArray data (Boyce et al., 2019). This study was able to interpret along strike variations in anomaly amplitude in the Grenville Province in the context of metasomatic modification of the edge of the Superior craton during protracted ( $\geq 300$  Ma) Proterozoic subduction. Now however, the recent USArray deployment in Alaska and neighboring temporary deployments in northern and western Canada (Figure 2 and Figure S4 in Supporting Information S1) mean that there is scope to significantly extend coverage everywhere north of the US-Canada border, illuminating the mantle beneath the contiguous U.S., through Canada and into Alaska. A resulting improved whole mantle North American P-wave model will consequently allow the address of a number of fundamental tectonic questions in western North America analogous to those in the Precambrian eastern domains. The high lateral resolution of P-wave tomography offers distinct advantages over the numerous existing S-wave models there.

In western Canada, a first order geomorphic observation is that the southern Canadian Cordillera occupies a relatively narrow band parallel to the coastline adjacent to the Precambrian interior, while farther north, the Mackenzie Mountains distort the Cordilleran Deformation Front (CDF) farther to the east in an arcuate shape (Figure 1). The morphological change in the Canadian Cordillera (CC) is incompletely understood but is colocated with the transition from a “lower-plate” to “upper-plate” type margin (analogous to the footwall and hanging wall) during the asymmetrical rifting of Laurentia (<720 Ma; e.g., Lund, 2008) and is reflected by changes in other seismological observables (Audet et al., 2016). Whether the surface geological expression of this transition extends below the crust is unconfirmed because until now such transfer zones have lacked a clear upper mantle expression in existing seismic tomographic models (e.g., Estève et al., 2019; Mercier et al., 2009; Schaeffer & Lebedev, 2014).

Further inland, the diamondiferous Archean Slave craton of northwestern Canada is flanked on the east and west by Proterozoic orogens (Figure 1) that are thought to have contributed to its modification through subduction driven metasomatism (e.g., C.-W. Chen et al., 2007; Aulbach et al., 2013; Eeken et al., 2018). However, the physical extent and compositional character of this modification is uncertain because petrological analyses are typically conducted on spatially limited xenolith samples (Aulbach et al., 2013; Heaman & Pearson, 2010) and variably resolving geophysical studies (Bostock, 1998; Bank et al., 2000; C.-W. Chen et al., 2007, 2009; Schaeffer & Lebedev, 2014; Eeken et al., 2018; Estève et al., 2019, 2020).

There is also scope for progress at mid-to-lower mantle depths. Models of the Mesozoic-to-Present subduction history of plates in western North America that formed the Proto-Pacific and their relation to the terminal formation of Alaska at  $\sim 50$  Ma suggest either dominantly eastward subduction below the North American plate in traditional reconstructions (e.g., Engebretson et al., 1985; Müller et al., 2019) or westward oceanic subduction below an offshore archipelago/ribbon continent west of North America (Johnston, 2008; Sigloch & Mihalynuk, 2017) prior to establishment of the modern-day regime. The newer theories (e.g., Clennett et al., 2020; Fuson & Wu, 2021; Sigloch & Mihalynuk, 2017) leverage high velocity anomalies (indicating cool subducted remnants) in the North American mid-mantle, some of which lie at the edge of present body wave tomographic model resolution (Burdick et al., 2017; Gou et al., 2019) meaning substantial debate remains (Clennett et al., 2020; Fuson & Wu, 2021).

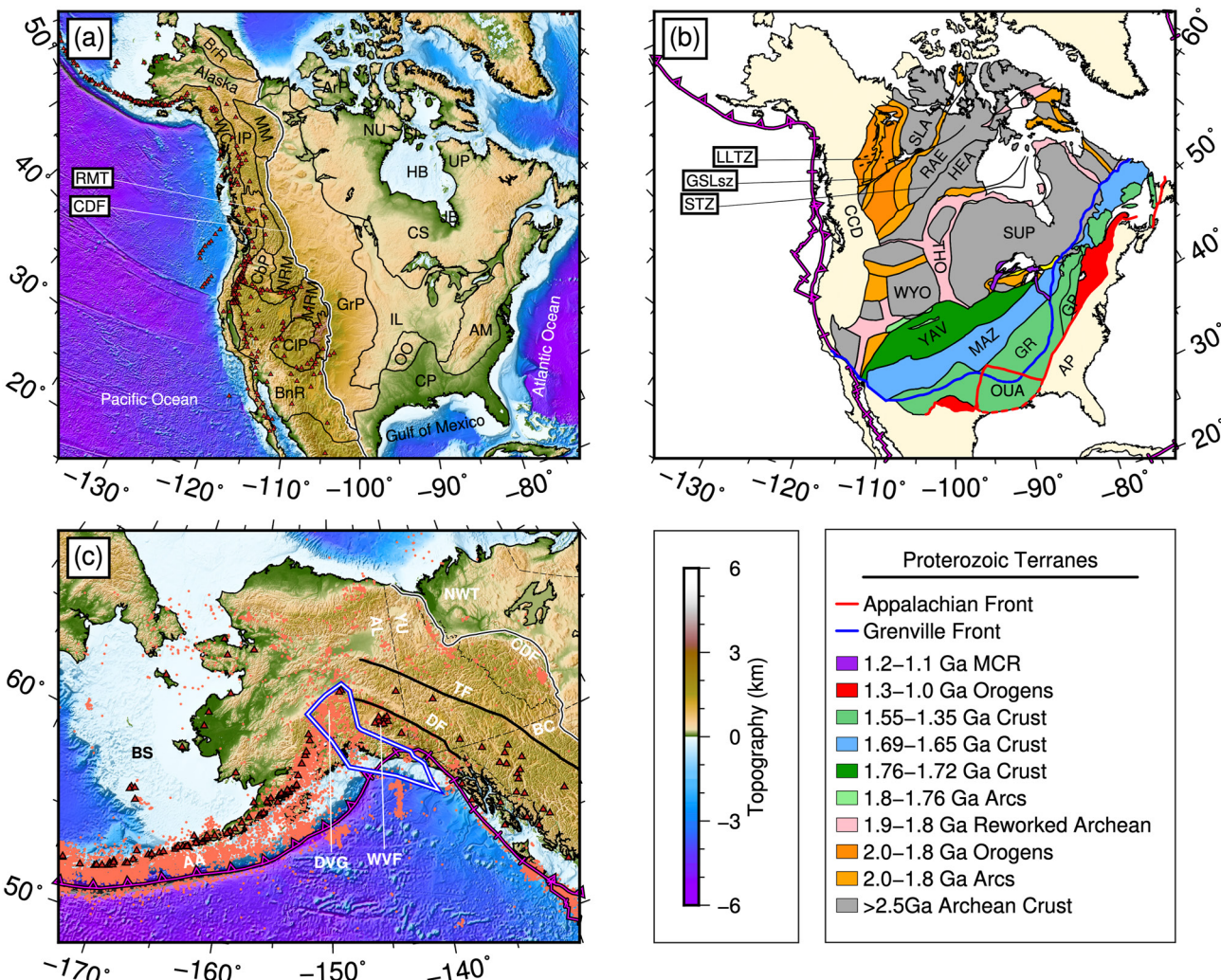


**Figure 1.** (a) North American topography and physiographic provinces. Quaternary volcanism: dark red triangles. ArP: Arctic Plains, BnR: Basin and Range, BrR: Brooks Range, CbP: Columbia Plateau, CDF: Cordilleran Deformation Front (highlighted), CIP: Colorado Plateau, CP: Coastal Plain, CS: Canadian Shield, GrP: Great Plains, HB: Hudson Bay, IL: Central Interior Lowlands, IP: Canadian Interior Plateaus, JB: James Bay, MM: Mackenzie Mountains, MRM: Middle Rocky Mountains, NRM: Northern Rocky Mountains, NU: Nunavut, OO: Ozark-Ouachita Highlands, RMT: Rocky Mountain Trench, SI: Southampton Island, UP: Ungava Peninsular, WC: Western Coastal Pacific Ranges. (b) Simplified basement geology (adapted after: Whitmeyer & Karlstrom, 2007). AP: Appalachian Province, CCD: Canadian Cordillera, GR: Granite-Rhyolite Province, GP: Grenville Province, GSLsz: Great Slave Lake shear zone, HEA: Hearne craton, LLTZ: Liard Line Transfer Zone, MAZ: Mazatzal Province, MCR: Mid-Continent Rift, RAE: Rae craton, SLA: Slave craton, STZ: Snowbird tectonic zone, SUP: Superior craton, THO: Trans-Hudson Orogen, WYO: Wyoming craton, YAV: Yavapai Province. Plate boundaries: magenta lines. (c) Alaskan tectonic features. Magnitude  $m_b \geq 4.0$  earthquakes 1971–2021: coral dots, Subducted Yakutat terrane: blue outline (after Eberhart-Phillips et al., 2006). Political boundaries; AL: Alaska, BC: British Columbia, NWT: North West Territories, YU: Yukon. Tectonic features; AA: Aleutian Arc, BS: Bering Sea, DF: Denali Fault, DVG: Denali Volcanic Gap, TF: Tintina Fault, WVF: Wrangell Volcanic Field.

Here, we use the Absolute Arrival-time Recovery Method (AARM: Boyce et al., 2017) to extract >186,000 absolute arrival-times from often-noisy temporary seismograph networks, to produce a North American P-wave tomography model (CAP22) with the highest resolution from the core-mantle boundary to the surface below Canada and Alaska to date. We focus our attention on tectonic processes at the margins of Precambrian domains in western Canada and new insights into subduction below Alaska.

## 1.2. Tectonic Setting

Continental North America comprises a collage of Archean cratonic blocks (>2.5 Ga) sutured by Proterozoic (2.5–0.6 Ga) collisional orogens, cross-cut by distinctive shear zones. The northwesterly craton amalgam includes the Slave craton (2.5–2.7 Ga), the Rae craton to the south east and the adjacent Hearne-Wyoming cratonic block

(Hoffman, 1988). The interspersed Proterozoic orogens within this tectonic assembly are scared by the Great Slave Lake shear zone intracontinental transform structure (e.g., Hamner et al., 1992; Hoffman, 1987) and the ~3,000 km Snowbird Tectonic Zone (Berman et al., 2007; Hoffman, 1988, see Figure 1). During the Palaeoproterozoic Trans-Hudson Orogen (THO - Figure 1; Hoffman, 1988; St-Onge et al., 2006) the 2.6–3.6 Ga Superior craton (e.g., Hoffman, 1988; Card, 1990, see Figure 1) collided with the Slave-Rae-Hearne amalgam. The THO stretches >4,600 km from central North America to Greenland, with much of its remnants residing beneath Hudson Bay. Southeast of the Superior craton, the central North American Proterozoic terranes (1.8–1.3 Ga e.g., Whitmeyer & Karlstrom, 2007) are bounded to the east by the 1.3–0.9 Ga Grenville orogen (e.g., Z. X. Li, Bogdanova, et al., 2008; Rivers, 2009; Hynes & Rivers, 2010), and subsequently the coastal Appalachian terranes (Hatcher, 2005, 2010; Van Staal, 2005). Igneous intrusions throughout southeast Canada and the offshore New England seamount chain are related to the Mesozoic (~190–110 Ma) Great Meteor hotspot (GMH; Sleep, 1990; Calvert & Ludden, 1999; Heaman & Kjarsgaard, 2000).

On the western side of the continent, the processes that led to the formation of the Cordilleran Orogen that stretches from California to the Alaskan Peninsula and abuts the stable continental interior are much less certain (e.g., Dickinson, 2004; Johnston, 2001, 2008; Monger, 1997; Sigloch & Mihalynuk, 2013). While only confident back to the mid-Cretaceous, traditional paleogeographic reconstructions based on ocean floor magnetic patterns and hot spot tracks (e.g., Engebretson et al., 1984; Engebretson et al., 1985) suggest that most of the building of the Cordillera was accommodated by a continual eastward subduction of ancestral Pacific lithosphere (e.g., Farallon plate) below western North America, in response to the opening of the Atlantic in the Jurassic. However, paleomagnetic studies show >3,000 km northward lateral displacement of Cordilleran rocks with respect to the stable North American interior (e.g., Beck & Noson, 1972), but geological evidence for such large offsets on currently known faults is lacking (e.g., Umhoefer, 2000), meaning the paleomagnetic measurements are challenging to reconcile with traditional plate reconstructions (e.g., Engebretson et al., 1984; Engebretson et al., 1985).

An alternative view suggests that the intraoceanic arcs and subduction complexes within the Cordillera are products of a two stage process in which (a) accretionary orogenesis in Triassic-Jurassic times resulting from westward subduction below an elongate continent or archipelago offshore western North America was followed by (b) continental collision of the elongate offshore terrane with North America and an outward stepping of subduction below the newly formed continental margin, below which subduction subsequently proceeded eastward (Johnston, 2001, 2008; Sigloch & Mihalynuk, 2013). This model allows for the large lateral displacements along the stable North American margin, better accounts for the distribution of subducted slabs in the North American mantle (e.g., Mezcalera and Angayucham slabs Sigloch & Mihalynuk, 2013; Sigloch & Mihalynuk, 2017; Clennett et al., 2020) and due to the presence of intraoceanic trenches, offers a more plausible explanation for Alaska's terminal formation at ~85–50 Ma (e.g., Johnston, 2001, 2008), compared to traditional models. Lateral translation of linear arcs and subsequent oroclinal buckling can therefore account for the “Z”- shaped geometry of today's central Alaskan mountains.

### 1.3. Previous Tomographic Insights

#### 1.3.1. North American Mantle: Shallow Structure

Global and continental scale P-wave models reveal fast wavespeeds ( $\delta V_p > 1\%$ ) throughout the Canadian shield and much of the central US at lithospheric depths (e.g., Montelli et al., 2006; C. Li, Van der Hilst, et al., 2008; Simmons et al., 2012; Schmandt & Lin, 2014; Burdick et al., 2017). Fast wavespeeds continue eastwards toward the Grenville Province and are sharply bounded by slow wavespeeds below the younger and tectonically active regions in western North America. The location of the western boundary of fast wavespeeds is better constrained by prior tomographic models compared to that to the east (e.g., Montelli et al., 2006; C. Li, Van der Hilst, et al., 2008; Simmons et al., 2012). However, Boyce et al. (2019) were recently able to show fast wavespeeds continuing eastwards to the Appalachian front in Canada, but limited to west of the Grenville Front farther south in the US, using a continental scale model with a focus on eastern North America. In comparison to the contiguous US, resolution often decays significantly, northwards into Canada where station coverage is less dense. Within the slow shallow wavespeeds below active western North America, a striking linear fast wavespeed anomaly is often imaged from ~40–50°N subparallel to the coastline at ~122°W, dipping to the east. This feature is typically associated with Juan de Fuca slab descent in the Cascadia subduction zone (e.g., Schmandt & Lin, 2014).

Early North American shear wavespeed models (e.g., Bedle & Van der Lee, 2009; Frederiksen et al., 2001; Grand, 1987; Nettles & Dziewonski, 2008; Van der Lee & Frederiksen, 2005) indicate fast wavespeed lithosphere

extends to 250–400 km depth, but show variable spatial correlation with surface tectonic domains. More recent surface wave models reveal fast wavespeeds ( $\delta V_s > 4\%$ ) throughout the lithosphere (to ~250 km depth) in the Canadian shield including the Archean Superior, Rae, Hearne and Slave cratons and adjoining Proterozoic domains. Fast wavespeeds continue eastwards throughout the Proterozoic Grenville Province, especially at shallower lithospheric depths ( $\leq 100$  km; Yuan et al., 2014; Schaeffer & Lebedev, 2014). Lower wavespeeds in the east are confined to the coastal Appalachian terranes where the lithosphere is thinner (Grand, 1987; Schaeffer & Lebedev, 2014). In the west, slow wavespeeds exist at upper mantle depths below the tectonically active US and Canadian Cordillera with the transition to the fast wavespeed interior closely following the Rocky Mountain Trench (RMT) and Cordilleran Deformation Front (CDF) from central America to northern Alaska (e.g., Schaeffer & Lebedev, 2014).

Careful attention has been paid to the location of lithospheric scale boundaries in regional scale seismic models (e.g., Bastow et al., 2015; Liddell et al., 2018). For example, in western Hudson Bay, Liddell et al. (2018) reveal no clear evidence for wavespeed variation between Paleoarchean Rae and Mesoarchean Hearne across the Snowbird Tectonic Zone (STZ). In eastern Canada, Boyce et al. (2016) revealed reduced seismic wavespeeds with decreasing tectonic age toward the coast between the Archean Superior, Proterozoic Grenville and Phanerozoic Appalachian terranes. In southwestern Canada, body waves have also been used to image the sharp transition from low-to-high wavespeeds below the RMT that may vary in dip direction along strike (Mercier et al., 2009; Y. Chen et al., 2018, 2019). In northwestern Canada, Estève et al. (2019, 2020) indicate that lower shallow mantle wavespeeds may continue to the east of the CDF, where the Archean Slave craton may have undergone metasomatic modification. However, these suggestions are difficult to confirm using relative arrival-times alone.

### 1.3.2. Alaskan Mantle

Broad-scale seismic tomographic models have typically lacked fine-scale resolution in Alaska, but as the USArray TA network expanded, a suite of new models arose (e.g., Burdick et al., 2017; Gou et al., 2019; Jiang et al., 2018; Martin-Short et al., 2016; Martin-Short et al., 2018). These studies typically reveal a fast wavespeed anomaly sub-parallel to the North America-Pacific plate boundary below the Alaskan peninsula. This anomaly, usually associated with the Alaskan slab, dips to the north, steepening to the east and terminates below south central Alaska with a sharp kink (e.g., Burdick et al., 2017; Martin-Short et al., 2016), below the proposed location of the eastern boundary of the Yakutat terrane. East of the Yakutat terrane lies the Wrangell Volcanic Field (WVF), whose provenance has been debated (e.g., Jadamec & Billen, 2010). Earlier studies conclude that there is little evidence for slab material below the WVF (e.g., Martin-Short et al., 2016, 2018; Qi et al., 2007; Wang & Tape, 2014), while more recent work suggests the extension of subducted material east of the Yakutat below the WVF (e.g., Daly et al., 2021; Gou et al., 2019; Jiang et al., 2018; Mann et al., 2022). Consensus shows the Alaskan slab has flattened in the lower mantle transition zone (~660 km depth; e.g., Qi et al., 2007; Burdick et al., 2017), which is also confirmed by receiver function analysis of the mantle transition zone (van Stiphout et al., 2019).

Many previous Alaskan tomographic studies suffer resolution loss at greater than ~400–600 km depth and toward northern Alaska due to a historical lack of station coverage. Consequently, only broad-scale and/or recent tomographic models resolve deeper fast wavespeed anomalies that hold clues to past subduction geometries (e.g., Clennett et al., 2020; Fuston & Wu, 2021). Based on published tomographic models, below northeast Alaska and northwest Yukon, Fuston and Wu (2021) suggest the presence of a “Yukon slab” detached from the main Alaska slab at ~300–500 km depth. Presently this feature is difficult to interpret alongside evidence for a deeper fast wavespeed anomaly offshore southern Alaska at ~800–1,500 km depth (e.g., Burdick et al., 2017; Hosseini et al., 2019), that instead may arise from Cretaceous intra-oceanic subduction south of Alaska (e.g., Clennett et al., 2020).

### 1.3.3. North American Mantle: Transition Zone and Below

Below a substantial portion of the contiguous US, fast wavespeeds extending laterally, centered at ~600 km depth are commonly interpreted as the flattening of the Farallon slab in the mantle transition zone following subduction below the western North American margin (e.g., Burdick et al., 2017; Grand, 1987; Schmandt & Lin, 2014; Sigloch, 2011). Deeper still, fast wavespeed anomalies extending vertically at various depths between 800 and 1,800 km were interpreted in the classical framework as deep continuation of Farallon eastward subduction (e.g., Sigloch, 2011). As discussed in Section 1.2, recent higher resolution imaging of deep mantle fast wavespeed

anomalies has reignited debate concerning the provenance of such proposed slab remnants (Clennett et al., 2020; Sigloch & Mihalynuk, 2013, 2017).

## 2. Body Wave Mantle Seismic Tomography

### 2.1. Absolute Arrival-Time Residuals

To constrain absolute P-wavespeeds throughout the mantle at continental scales, global and regional absolute arrival-time data sets are required to resolve both subducted slabs (e.g., Sigloch, 2011) and lithospheric boundaries (e.g., Boyce et al., 2019). We use the global “EHB” database (Engdahl et al., 1998) recorded from 1964 to 2004 (e.g., C. Li, Van der Hilst, et al., 2008) and USArray Transportable Array (TA) data recorded from 2004 to 2020 (updated from Astiz et al., 2014; Burdick et al., 2017) providing absolute arrival-time picks for phases P, Pn, Pg, pP, PKP, and PKIKP (see Figures S1–S3 in Supporting Information S1). Canadian station distribution within the global database is sparse and a great number of networks in Alaska are rarely used, so we supplement EHB and TA data with other temporary networks in Canada and Alaska. Data from station networks active during the period 2005–2020 were accessed via IRIS and the Canadian National Data Center databases. We exclude stations associated with glacial monitoring to avoid possible travel-time inaccuracies.

Seismic data are extracted from the following specific networks, with more details available in the Open Research Section and Supporting Information S1: AK-1987 (Alaska Earthquake Center, Univ. of Alaska Fairbanks, 1987; D’Alessandro & Ruppert, 2012), AT-1967 (NOAA National Oceanic and Atmospheric Administration (USA), 1967; Oppenheimer et al., 2005), AV-1988 (Alaska Volcano Observatory/USGS, 1988; Dixon et al., 2013), CN-1975 (Natural Resources Canada (NRCCAN Canada), 1975; North, 1994; Bent et al., 2019), C8-2002 (Natural Resources Canada (NRCCAN Canada), 2002), EO-2018 (University of Calgary (U of C Canada), 2018; Boggs et al., 2018), GM-2016 (U.S. Geological Survey, 2016; Ringler et al., 2021), II-1986 (Ringler et al., 2021; Scripps Institution of Oceanography, 1986), IM-1965 (Ringler et al., 2021; Various Authors, 1965), IU-2014 (Albuquerque Seismological Laboratory/USGS, 2014; Ringler et al., 2021), NY-2013 (University of Ottawa (uOttawa Canada), 2013; Estève et al., 2020), OO-2013 (Rutgers University, 2013), PO-2000 (Eaton et al., 2004; Geological Survey of Canada, 2000; Snyder et al., 2003), PN-1998 (Indiana University Bloomington (IU Bloomington), 1998), RV-2013 (Alberta Geological Survey / Alberta Energy Regulator, 2013; Schultz et al., 2015), TD-2013 (TransAlta Corporation, 2013; Cui & Atkinson, 2016), US-1990 (Albuquerque Seismological Laboratory (ASL)/USGS, 1990; Ringler et al., 2021), XL-2017 (McGill University (Canada), 2017; Roth et al., 2020), XM-2011 (Keranen, 2011), XN-2003 (Gaherty & Revenaugh, 2003; Mercier et al., 2009), XO-2018 (Abers et al., 2018; Barchek et al., 2020), XR-2004 (Song & Christensen, 2004), XV-2007 (Larsen & Truffer, 2007), XY-2005 (Calkins et al., 2010; Dueker & Zandt, 2005), XZ-2005 (Berger et al., 2008; Hansen & Pavlis, 2005), X5-2007 (University of Bristol (UK), 2007; Bastow et al., 2015), X9-2012 (Nabelek & Braunmiller, 2012), YO-2016 (Yukon Geological Survey, 2016; Estève et al., 2019), Y5-2006 (University of Alberta (UAlberta Canada), 2006; Gu et al., 2011), ZE-2015 (Tape et al., 2015, 2017), Z5-2013 (Nabelek & Braunmiller, 2013), 1E-2018 (Natural Resources Canada (NRCCAN Canada), 2018; Babaie Mahani et al., 2019), 2K-2014 (Schultz et al., 2014, 2020), 7A-2010 (Woods Hole Oceanographic Institution (WHOI), 2010), 7C-2015 (Baker et al., 2020; Schutt & Aster, 2015), 7D-2011 (IRIS OBSIP, 2011; Toomey et al., 2014).

To obtain absolute arrival-time picks from often noisy regional temporary deployments we follow the two-step approach outlined by Boyce et al. (2019, 2021). First, networks are split into sub-regions of less than a few thousand kilometers aperture (Figure S4 in Supporting Information S1); Alaska OBS (Alaskan Ocean-Bottom Seismometers ALO), Alaska land-stations (ALS), Alaska volcano network (ALV), Hudson Bay (HSB), Northwest Canada (NWC), Southwest Canada (SWC), Western US—Cascadia—OBS (WUO). Data processing within each sub-region is near identical to ensure compatibility of final picks, the only differences being where we capitalize on previously processed relative arrival-time data sets where available (Estève et al., 2020; Liddell et al., 2018). We calculate relative arrival-times separately within each region using Multi-Channel Cross-correlation (VanDecar & Crosson, 1990) for all sub-regions excluding NWC and HSB. For NWC we repick the relative arrival-times of Estève et al. (2020) spanning 2002–2018 but exclude the USArray TA data (because we take these picks from the TA data set), to ensure compatibility with our processing. We take directly the relative arrival-times of Liddell et al. (2018), calculated following Rawlinson and Kennett (2004), spanning 2004–2015 into step two. In step two, we apply the AARM (Boyce et al., 2017) to each sub-region data set to obtain absolute arrival-time picks compatible with EHB and TA databases. In this approach, we optimally stack the unfiltered raw data based on alignments

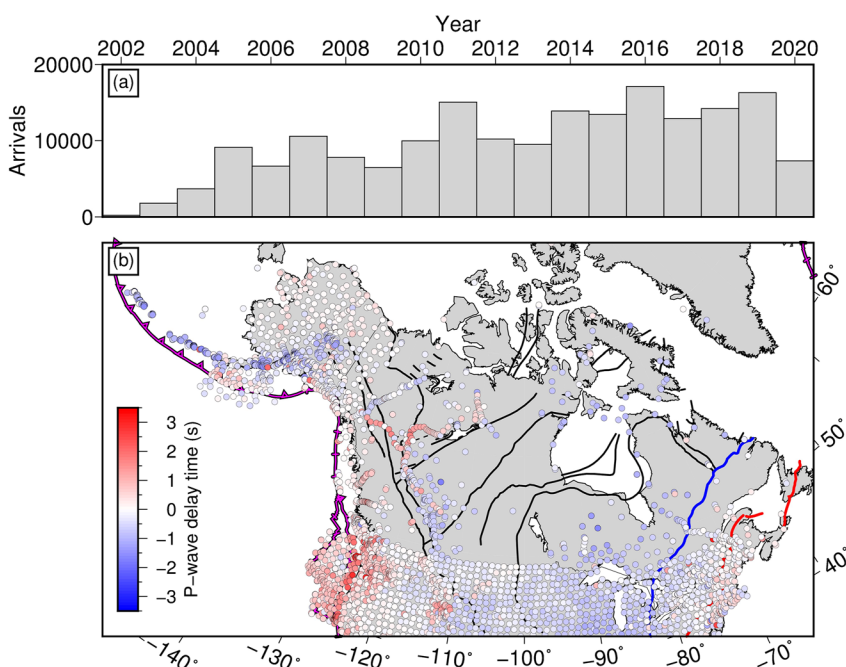


**Figure 2.** (a) Temporal distribution of new arrival-time measurements used in this study. (b) Mean P-wave absolute arrival-time residuals derived from the following databases: EHB (C. Li, Van der Hilst, et al., 2008); USArray TA (updated from Burdick et al., 2017), BBNAP19 (Boyce et al., 2019); new CAP22 data set added here. Residuals are corrected for Earth's ellipticity and station elevation. Structural boundaries as in Figure 1.

derived from the relative arrival-time step to reveal the first-break or onset time of the P-wave above the noise on the resulting high SNR stack. This enables accurate absolute arrival-times to be extracted for each station across the sub-region. For further information on the details of this procedure, please see Supporting Information S1 (Figures S4–S18 in Supporting Information S1) and previous work (Boyce et al., 2017, 2019, 2021). For completeness, we include the 16,397 absolute arrival-time picks of Boyce et al. (2019) in southeastern Canada. Our total absolute arrival-time data set comprises 202,719 picks from temporary seismograph stations across Canada and Alaska.

Travel-time data are corrected for Earth's ellipticity using the formulation of Kennett and Gudmundsson (1996) and station elevation accounting for ray incidence angles. Figure 2 shows mean P-wave absolute arrival-time residuals with respect to ak135 (Kennett et al., 1995). While absolute arrival-times document wavespeed variations along the entire ray path, first order trends resulting from upper mantle structure can be uncovered when large data sets are averaged over a broad back azimuthal distribution. Earlier arrivals are observed throughout the Precambrian continental US, west of the Grenville Front, up to the active western region where residuals are typically delayed or around the global mean. Mean station residuals show early arrivals that dominate southeast Canada (Boyce et al., 2019) and continue northwards of Hudson Bay ( $\sim 1$  s) with little spatial variation. In southwest Canada, west of the CDF below the Canadian Cordillera, residuals are often around the global mean to slightly delayed ( $\sim 0$ – $0.75$  s). East of the CDF, residuals are typically earlier than expected ( $\leq -0.75$  s), in agreement with Y. Chen et al. (2018). A marked change in residuals is observed approximately coincident with the LLTZ and GSLsz in northwest Canada. North of this boundary, delayed arrivals are observed both west of the CDF below the Cordillera and also continuing beyond the CDF to the east through the Proterozoic orogens (up to 1.75 s delay), toward the Slave craton ( $\sim 0.75$  s delay). By contrast, residuals below the northern Mackenzie Mountains are of opposite sign ( $-1.0$ – $0$  s). The TA data set reveals low amplitude residuals throughout western Yukon, northern and central Alaska. In southern Alaska and along the Aleutian Arc, residuals are often earlier than expected ( $\sim 1.5$  s).

## 2.2. Absolute P-Wavespeed Tomographic Inversion

Prior to tomographic inversion, we undertake two final processing steps. Firstly, the potentially significant impact of the crust (e.g., Waldhauser et al., 2002) is accounted for using the  $1^\circ \times 1^\circ$  degree resolution North American

crustal model NACr14 (Tesauro et al., 2014). We wish to avoid the introduction of artifacts at boundaries in coverage that may result from using other regional or bespoke patchwork crustal models. We project NACr14 onto the parameterized inversion grid, propagate rays through this crustal model and remove the arrival-time residual produced by the crust from the data. Secondly, to limit the impact of converging lines of longitude at high latitudes, we employ a coordinate transformation to translate our study region to equatorial latitudes resulting in regular grid cell shapes throughout North America (See Figure S19 in Supporting Information S1).

Absolute P-wave arrival-time data are inverted for slowness perturbations with respect to ak135 and hypocenter mislocation parameters following the iterative, linearized, least squares inversion approach of C. Li, Van der Hilst, et al. (2008); Burdick et al. (2017). Theoretical travel times and ray paths are calculated by ray tracing through the spherically symmetric (1-D) ak135 reference model Kennett et al. (1995), prior to clustering into weighted composite rays according to station and earthquake density (Káráson & Van der Hilst, 2001). The size of an event cluster in our composite ray approach can approach a maximum of 26.1 km in latitude and longitude, and 15.1 km in depth, far greater than anticipated uncertainties in the earthquake catalog. Subsequently, the cells within the regularly parameterized global grid (45 km in depth, 0.35° in latitude and longitude) are combined with adjacent cells according to ray density (minimum 900 rays per cell; Figure S20 in Supporting Information S1). Our approach minimizes the cost function:

$$\epsilon = w\|Gm - d\|^2 + \lambda_1\|Lm\|^2 + \lambda_2\|m\|^2. \quad (1)$$

Differences between the observed data  $d$  and predictions, estimated by the sensitivity matrix  $G$  and model,  $m$ , are weighted by  $w$  in the first term. Use of the infinite frequency approximation means  $G$  consists of the length of each composite ray in each cell and partial derivatives for hypocentral parameters (e.g., Káráson & Van der Hilst, 2001; Nolet, 1987; Spakman & Nolet, 1988). We give AARM derived data sets three times greater weighting than EHB and TA data sets following Boyce et al. (2019) to compensate for the different sizes of each data set. The inversion is regularized by a first derivative smoothing constraint in both horizontal and vertical directions ( $L$  - second term) and is damped by the model norm (third term). Trade-off analysis is used to choose the weights for these terms  $\lambda_i$  (Figure S21 in Supporting Information S1). We systematically vary the horizontal gradient smoothing (Figure S21a in Supporting Information S1), the vertical gradient smoothing (Figure S21b in Supporting Information S1), and both together to select an appropriate model close to the bend in the trade-off curve, although we prefer a smoother model to better mitigate the effects of data sets of differing size and weights across the US-Canada border specifically. The model damping parameter has very limited impact on the resulting model around the bend in the trade-off curve. We run 400 iterations although the inversion converges well beforehand. The standard deviation of cluster hypocentral mislocation terms resulting from inversion are 0.74° in longitude, 0.87° in latitude, 1.01 km in depth, and 1.03 s in time.

### 2.3. Tomographic Resolution Assessment

We conduct checkerboard tests appropriate for continental and Alaskan scales (Figures 3 and 4, Figures S22–S24 in Supporting Information S1) and a continental synthetic structural test (Figure 5) motivated by the distribution of absolute arrival-time residuals (Figure 2) and our final inversion. For checkerboard test inputs, we distribute alternating  $\delta V_p = \pm 2\%$  wavespeed anomalies of 300 km thickness and 1°–10° width throughout the model space centered at 200, 500 and 800 km depth. We calculate arrival-time residuals through synthetic wavespeed models, using identical ray paths to the observed data. Based on estimated absolute arrival-time pick errors (Figures S12–S18 in Supporting Information S1), we add 0.2 s standard deviation Gaussian noise to the synthetic data before inversion.

Throughout the contiguous US and Alaska, anomalies of 5° width show excellent spatial recovery at all depths (>75% amplitude, Figure 3). Compared to the eastern coastline, anomalies off the west coast of the US/Canada and southern Alaska display improving recovery with depth, aided by offshore OBS station deployments. In western Canada, recovery of 5° anomalies is also good (>40% amplitude) below station coverage. Central and northeastern Canada displays weaker recovery of 5° anomalies at 200 km depth but anomalies are located reasonably well in southeastern Canada. Below Alaska, western Canada and the contiguous US, the boundaries between 10° anomalies are accurately recovered at 200–800 km depth with anomaly amplitude recovery largely >40% below the continental region (Figure S22 in Supporting Information S1). Recovery of anomalies below Hudson Bay and northeast and central Canada is weak at 200–500 km depth where anomalies exhibit some lateral

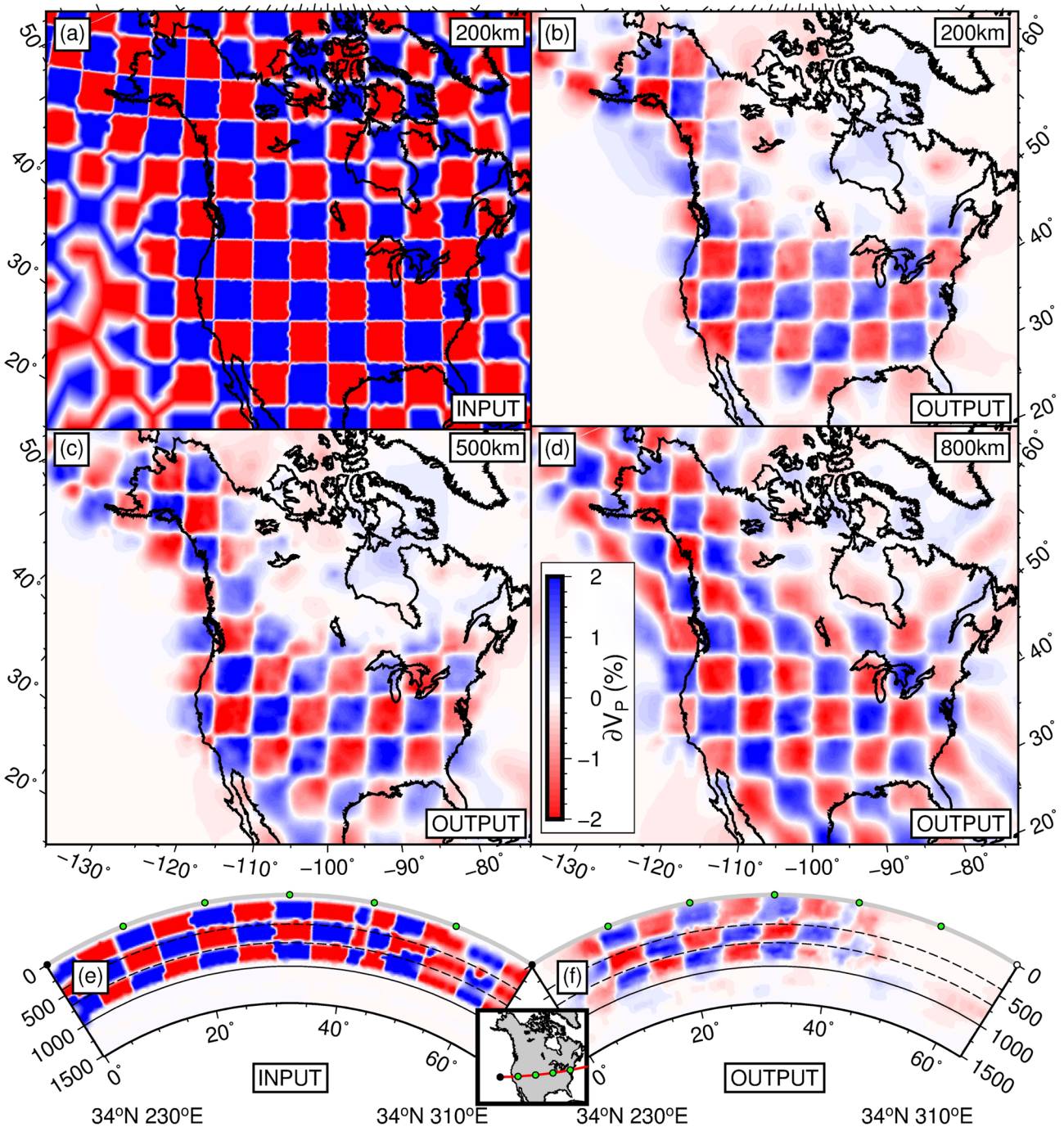


**Figure 3.** Checkerboard resolution tests using  $\delta V_p = \pm 2.0\%$  input wavespeed anomalies of  $5^\circ$  width. Positive and negative input anomalies arranged in an alternating grid at 200, 500 and 800 km depth are displayed in map (a) and cross section along the W-E profile (e). Visual defects within the input anomaly model result from a coarse adaptive grid in poorly sampled regions (Figure S20 in Supporting Information S1). Recovered anomalies (b–d, f) are displayed on the same color scale as the input.

smearing. All checkerboard anomalies below central Canada are better recovered at 800 km depth. Depth resolution throughout the continental US is good with very limited vertical smearing of anomalies (<100 km; Figure 3, Figure S22 in Supporting Information S1).

Lateral resolution of  $2^\circ$ – $3^\circ$  anomalies below Alaska and the Alaskan peninsula (200–500 km depth) is excellent with amplitude recovery typically  $>70\%$  (Figure 4 and Figure S23 in Supporting Information S1). Amplitude

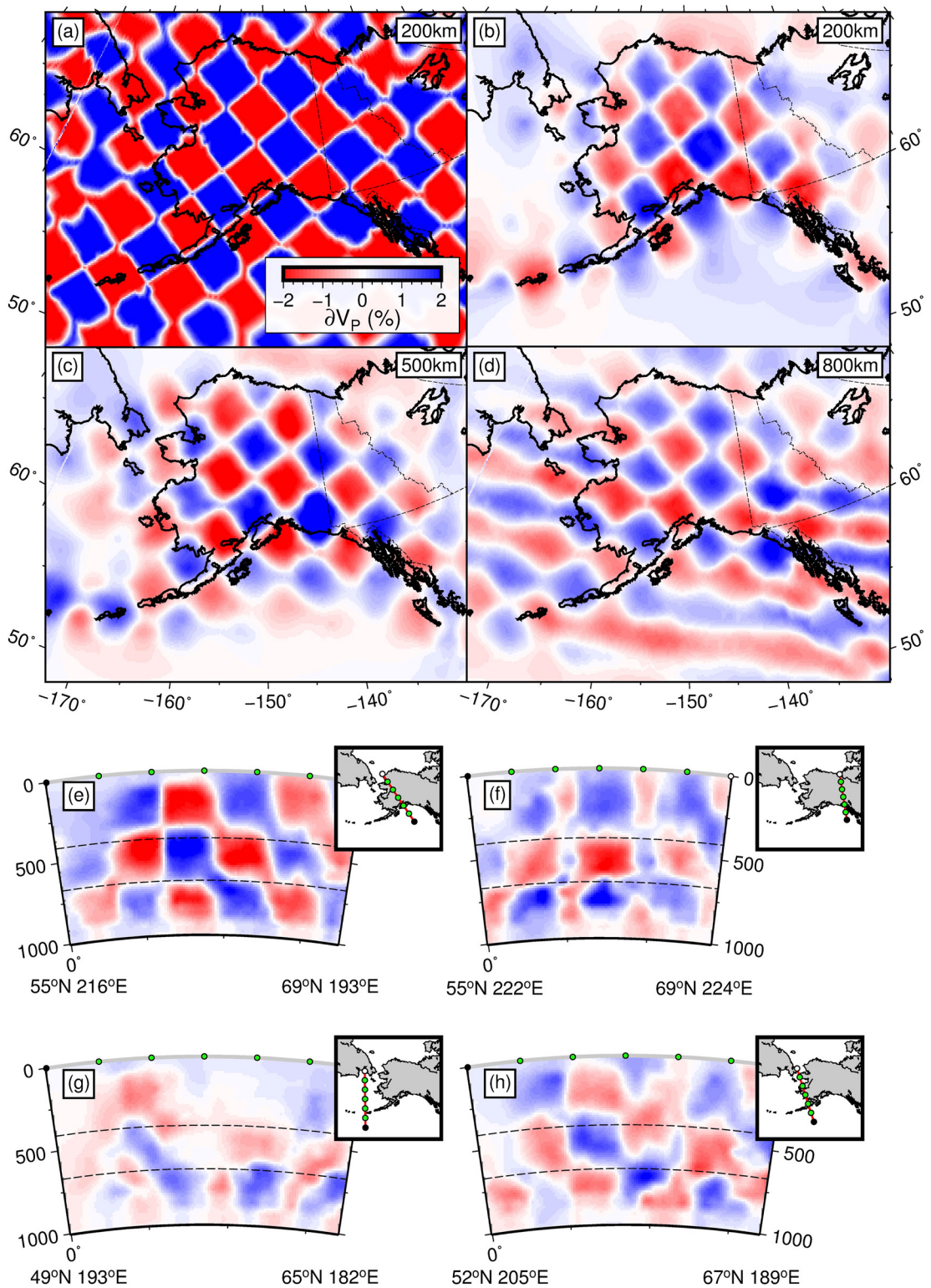


**Figure 4.** Checkerboard resolution tests shown for Alaska using  $\delta V_p = \pm 2.0\%$  input wavespeed anomalies of  $3^\circ$  width. Positive and negative input anomalies arranged in an alternating grid centered at 200, 500 and 800 km depth are displayed in map view (a). Visual defects within the input anomaly model result from a coarse adaptive grid in poorly sampled regions (Figure S20 in Supporting Information S1). Recovered anomalies (b–h) are displayed on the same color scale as the input. We use the same cross-sections as Figure 11 to assist comparison.

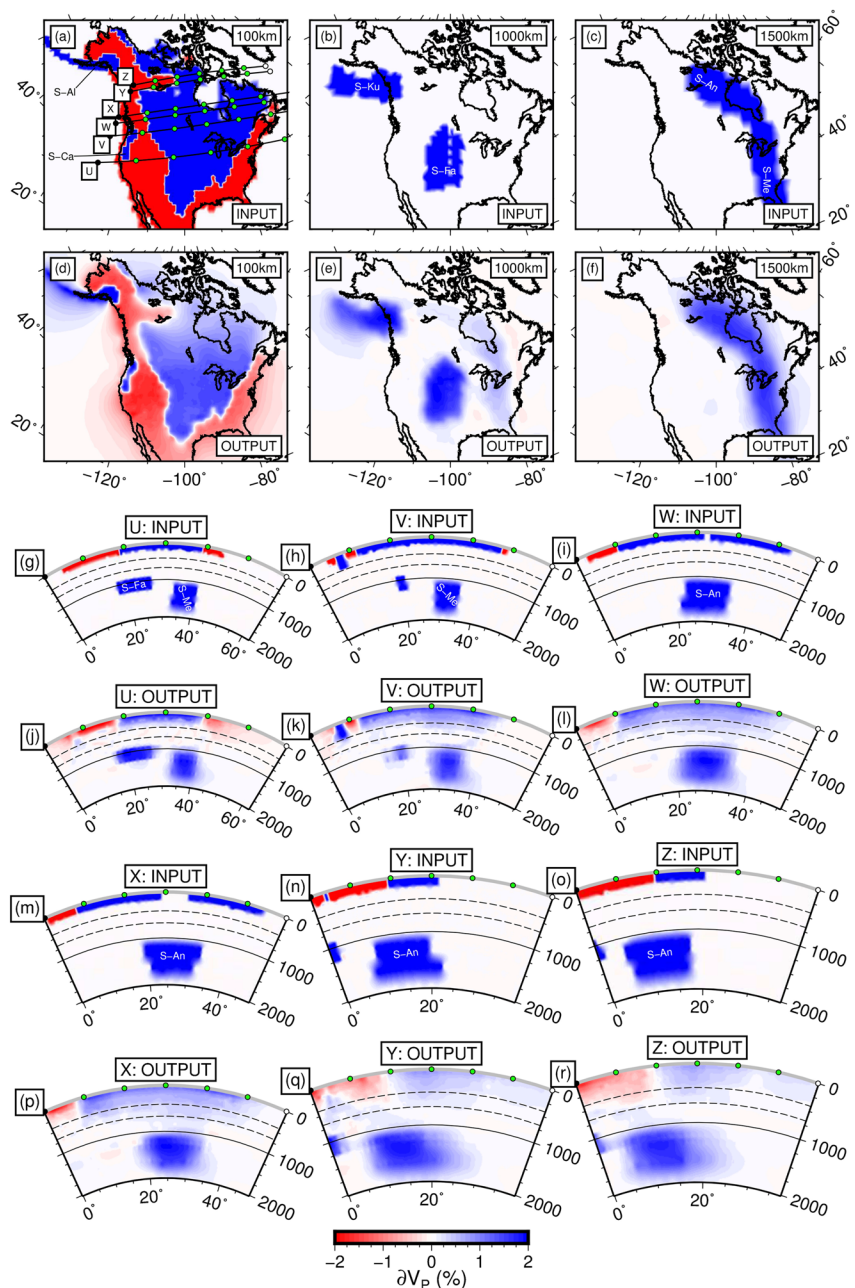


**Figure 5.** Structural resolution test for North America based on approximate fast and slow wavespeed anomalies in the upper mantle (0–200 km depth) and simple subducted slabs in the upper (0–400 km depth) and mid-to-lower (900–1,900 km depth) mantle of the CAP22 tomographic model. Input slab anomalies: S-Al: Alaskan slab, S-Ca: Cascadia slab, S-Ku: Kula slab, S-Fa: Farallon slab, S-An: Angayucham slab, S-Me: Mezcalera slab. Visual defects within the input anomaly model result from a coarse adaptive grid in poorly sampled regions (Figure S20 in Supporting Information S1). Input anomaly amplitudes are  $\delta V_p = \pm 2.0\%$ . Input-Output pairs are displayed in map (a–f) and cross section (g–r). Cross section locations (U–Z) are shown in (a).

recovery decreases slightly toward the north and below 500 km depth. Lateral resolution of  $3^\circ$  anomalies in western Yukon matches that found in Alaska but decays for anomalies of  $2^\circ$ . Vertical resolution below south-central Alaska is excellent for  $2^\circ$ – $3^\circ$  anomalies but worsens elsewhere. Figure S24 in Supporting Information S1 shows lateral resolution may approach  $1^\circ$  in the upper mantle below south central Alaska.

Structural resolution testing (Figure 5) shows anomaly amplitude recovery at lithospheric depths in US is  $>60\%$ , with excellent lateral resolution of wavespeed boundaries, although wavespeeds do smear laterally away from

the coast. Vertical smearing is also relatively limited in extent (100–200 km). Spatial recovery of input slab anomalies S-Al and S-Ca is also good at shallow depth below the continent, but fast wavespeeds are smeared laterally to the south from S-Al from below the Alaskan peninsula and Aleutian Arc (Figures 5d and 5k). Vertical smearing of anomaly S-Ca (0–400 km depth input) is ~100 km. Below much of Canada, amplitude recovery of fast and slow anomalies is >40% but decays below central and northern regions where station density is sparse. Lateral recovery of lithospheric depth wavespeed boundaries is also good below Canada but some short wavelength heterogeneity is smoothed laterally, for instance in northwestern Canada. Fast wavespeeds are smeared laterally across Hudson Bay. Lithospheric scale anomalies (0–200 km depth input) can be vertically smeared to below 400 km depth across Canada but smeared amplitudes decay significantly with depth. At ~1,000 km depth, mid-mantle input slab anomalies S-Ku and S-Fa exhibit good recovery with amplitudes >80%, however the southwestern-most extent of S-Ku is uncertain (Figures 5e and 5j). Below 1,000 km depth, lower mantle input slab anomalies S-An and S-Me are well recovered (amplitudes >60%) but smear more strongly laterally than vertically (Figures 5f, 5j–5l, 5p–5r).

While the imperfect nature of checkerboard tests is well documented (Rawlinson & Spakman, 2016), they can be used to quantitatively ascertain which regions within CAP22 are resolved at a given length scale using the approach of Burdick et al. (2014). The input  $5^\circ$  checkerboard model,  $m_0$ , is compared to the recovered model,  $m$ , to define a resolving power  $R$ :

$$R = \frac{[(m - m_0)^T W(m - m_0)]^{1/2}}{(m_0^T W m_0)^{1/2}}. \quad (2)$$

$W$  defines a Gaussian function that smoothly weights the contribution from adjacent cells in the  $5^\circ$  checkerboard. Resolved regions are found where  $R > 0.25$  and thus regions outside this are grayed out (e.g., Figures 6–8). From our tests we conclude that lateral resolution is sufficient to resolve lithospheric scale wavespeed boundaries throughout the contiguous US, Alaska, western and southeastern Canada and broad-scale mid-mantle slab remnants. In Section 3.2 we specifically discuss features resolved by newly added temporary network data rather than by EHB and TA data sets.

### 3. Results and Comparisons With Previous Studies

#### 3.1. Tomographic Results

At upper mantle depths ( $\leq 300$  km), the Precambrian interior of North America is dominated by fast wavespeeds ( $\delta V_p > 0.5\%$ ) in CAP22 (Figures 6 and 7). The Appalachians, Coastal Plains, and tectonically active regions west of the Great Plains, are broadly characterized by slow wavespeeds ( $\delta V_p < -0.75\%$ ). Fast wavespeed anomalies are interspersed between locations of Cenozoic volcanism or are associated with the Cascadia subduction system. At greater depth (600–1,800 km), distinct fast wavespeed anomalies (Figures 8 and 9) are likely products of complex subduction associated with the westward drift of North America since the Cretaceous (e.g., Clennett et al., 2020; Engebretson et al., 1985; Sigloch & Mihalynuk, 2013). In the subsequent sections we focus on Canada and Alaska where new data provide significant resolution improvement over earlier studies.

##### 3.1.1. Canada

Upper mantle wavespeeds in CAP22 (Figures 6 and 7) broadly reflect the distribution of absolute arrival-time residuals across Canada (Figure 2). The wavespeed pattern is largely independent of the crustal model used (e.g., NACr14, CRUST1.0; Laske et al., 2013; Tesauro et al., 2014), only amplitudes change appreciably when crustal models are varied.

In southeast Canada, fast wavespeeds are imaged throughout the upper mantle below the Superior craton, with wavespeeds decreasing through the Grenville Province and into the Appalachians toward the coast where slow wavespeeds are more prevalent. Fast wavespeed amplitudes within the Superior are muted below the Great Meteor Hotspot track west of James Bay (Figure 6). Low station density in northeast Canada inhibits good resolution of detailed structures but CAP22 displays broad fast wavespeeds in northern Hudson Bay stretching from Nunavut, across Southampton Island into the Ungava Peninsula and northern Superior ( $\delta V_p > 0.4\%$ ; Figures 6, 7 and 10). Likely due to some vertical smearing, fast wavespeeds in eastern Canada extend below an apparent depth of ~400 km. In central Canada, below large parts of the THO and Hearne craton, stations are lacking thus we

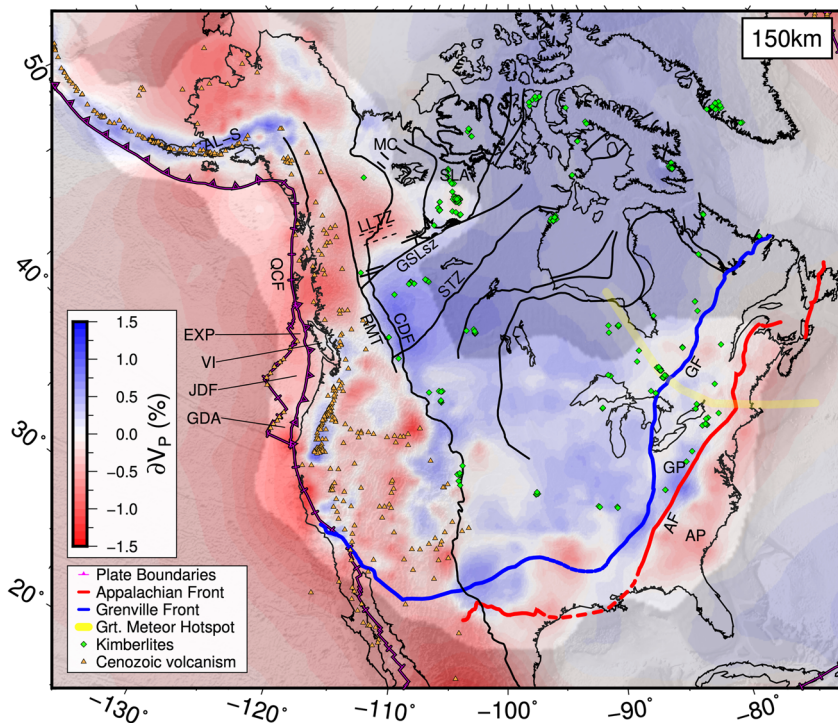


**Figure 6.** CAP22 tomographic model at 150 km depth, plotted as deviation from ak135 over topographic shading. Gray areas are unresolved according to recovery of 5° checkerboard anomalies (following Burdick et al., 2014, See Section 2.3). AF: Appalachian Front, AL-S: Alaskan slab, AP: Appalachian Province, CDF: Cordilleran Deformation Front, EXP: Explorer plate, GDA: Gorda plate, GF: Grenville Front, GP: Grenville Province, GSLsz: Great Slave Lake shear zone, JDF: Juan de Fuca plate, LLTZ: Liard Line Transfer Zone, MC: Possible location of Mackenzie Craton, QCF: Queen Charlotte Fault, RMT: Rocky Mountain Trench, SLA: Slave craton, STZ: Snowbird tectonic zone VI: Vancouver Island. Other structural boundaries as Figure 1.

choose not to interpret wavespeed variations in these poorly resolved regions at upper mantle depths. At greater depth ( $\sim 1,200\text{--}1,800$  km), a broad fast wavespeed anomaly ( $\delta V_p > 0.3\%$ ) oriented northwest-southeast continues from the Appalachian coast toward northwest Canada (Figures 8 and 9).

North of the Cascadia subduction system, below the Cordillera in southwest Canada, slow wavespeeds ( $\delta V_p < -0.5\%$ ) continue inland from the coast terminating abruptly at the RMT, east of which wavespeeds are fast ( $0.5\% \leq \delta V_p \leq 1.0\%$ ) below Precambrian domains at upper mantle depths ( $\sim 100\text{--}300$  km; Figures 6 and 7). Below the RMT in southwest Canada, the slow-to-fast wavespeed boundary dips slightly westward (Figures 10b and 10d). Below the shallow mantle, correlations with lithospheric scale boundaries are lost and patches of slow and fast wavespeeds are found, transitioning into slow wavespeeds at mid-mantle depths ( $>1,000$  km; Figures 8 and 9). Slow upper mantle wavespeeds exist below the CCD and MM in northwest Canada ( $\delta V_p < -0.5\%$ ), but instead of terminating at the RMT or Tintina fault, continue beyond the CDF in the southern Mackenzie Mountains, eastwards through Proterozoic orogenic belts toward the Slave craton (Figures 6 and 7). This wavespeed transition occurs north of the GSLsz, at the LLTZ. Peak slow wavespeeds below the central Slave craton occur at 100 km depth ( $\delta V_p \approx -0.3\%$ ) but reduce in anomaly amplitude with depth, and are extinguished below 200 km depth. By contrast, the transition to fast wavespeeds ( $\delta V_p \geq 0.3\%$ ) occurs closer to CDF in the northern Mackenzie Mountains of northwest Yukon and Northwest Territories (NWT—see Figures 1c and 11) at 100–300 km depth. Below the upper mantle, slow wavespeeds are also broadly distributed in northwest Canada but are interrupted by a fast wavespeed elongate anomaly that continues from northern British Columbia offshore to the southwest ( $\sim 600\text{--}800$  km depth). This feature broadens and continues to the west at greater depth ( $\sim 1,000\text{--}1,200$  km,  $\delta V_p > 0.5\%$ ; Figure 8) offshore southern Alaska. At  $\sim 1,200\text{--}2,000$  km depth, CAP22 resolves the western limit of the broad fast wavespeed anomaly orientated northwest-southeast ( $\delta V_p > 0.3\%$ ) extending between southeastern Canada and northern Yukon (Figure 9).

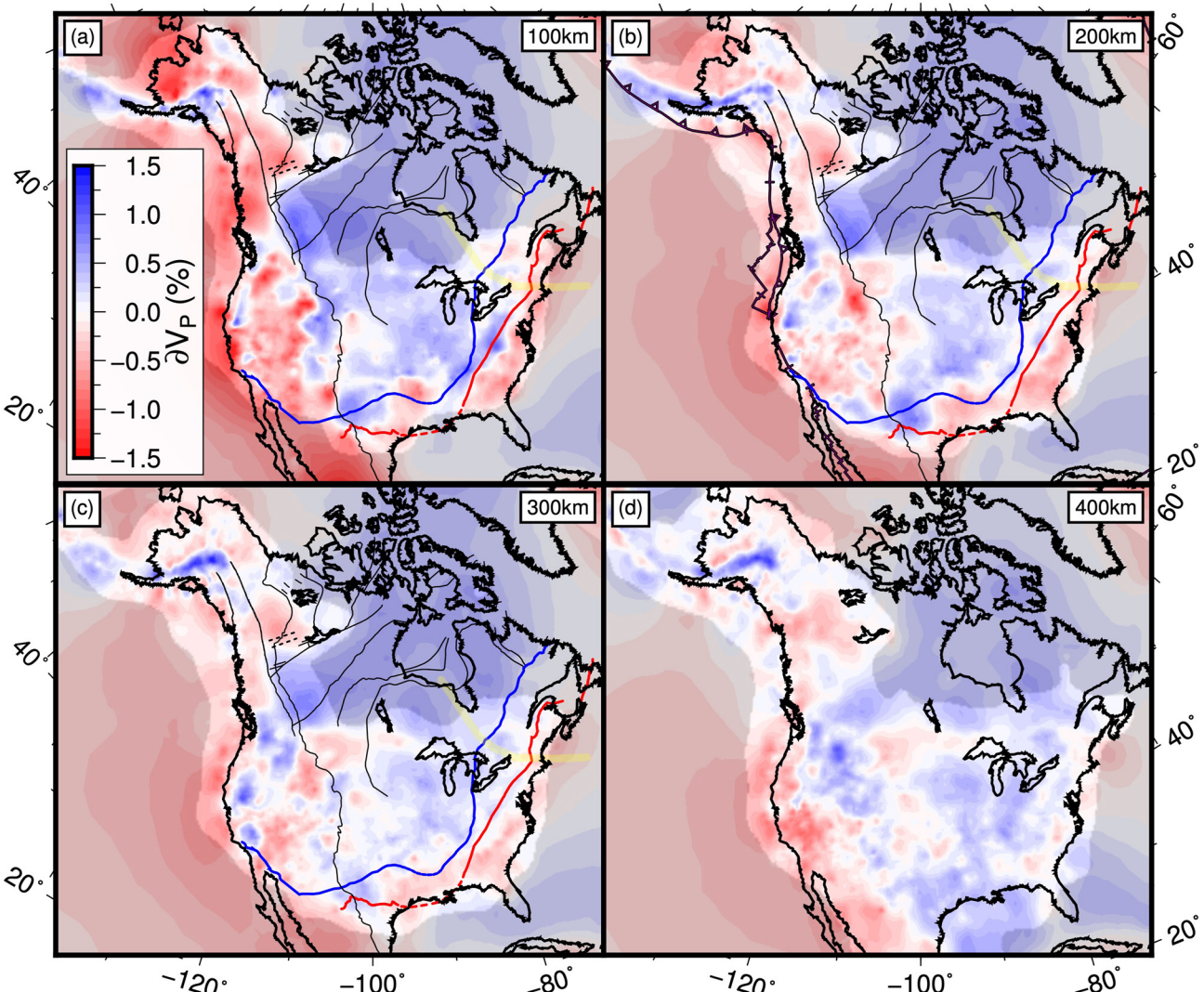


**Figure 7.** CAP22 tomographic model at upper mantle depths of 100–400 km (a–d), plotted as deviation from ak135. Gray regions are unresolved according to recovery of  $5^\circ$  checkerboard anomalies (following Burdick et al., 2014, See Section 2.3). Structural boundaries as Figure 1.

### 3.1.2. Alaska

Shallow mantle wavespeeds in western to northeastern Alaska are predominantly slow ( $-0.5\% \geq \delta V_p \geq -1.5\%$ ) with the most pronounced fast wavespeed anomaly occurring at 100 km depth below central Alaska and the Brooks Ranges. In south-central Alaska at upper mantle depths, fast wavespeeds ( $\delta V_p > 0.5\%$ ) are broadly distributed with a possible gap in fast wavespeeds below the Yakutat terrane at 200 km depth (Figures 11b and 11e) that interrupts the line of recent volcanism at the DVG. To the west, the subducting Pacific plate is delineated by a fast wavespeed arcuate anomaly, sub-parallel to the trench. This anomaly is broadly continuous in depth (100–400 km). At  $\sim 400$  km depth, low-amplitude, fast wavespeed anomalies ( $\delta V_p \approx 0.25\%$ ) also exist below northwest Alaska and also northeast Alaska/northwest Yukon and NWT (Figures 11c and 11f). At  $\sim 600$  km depth, fast wavespeeds are less continuous below the Aleutian arc but spread laterally below southwest Alaska and Bering Sea (Figures 11d, 11g and 11h).

### 3.2. Data Set Contributions

We analyze the contribution of “EHB-TA” data compared to temporary network data (unique to CAP22 and Boyce et al., 2019, “CAP22-only”) in facilitating resolution of features throughout the mantle. We perform two

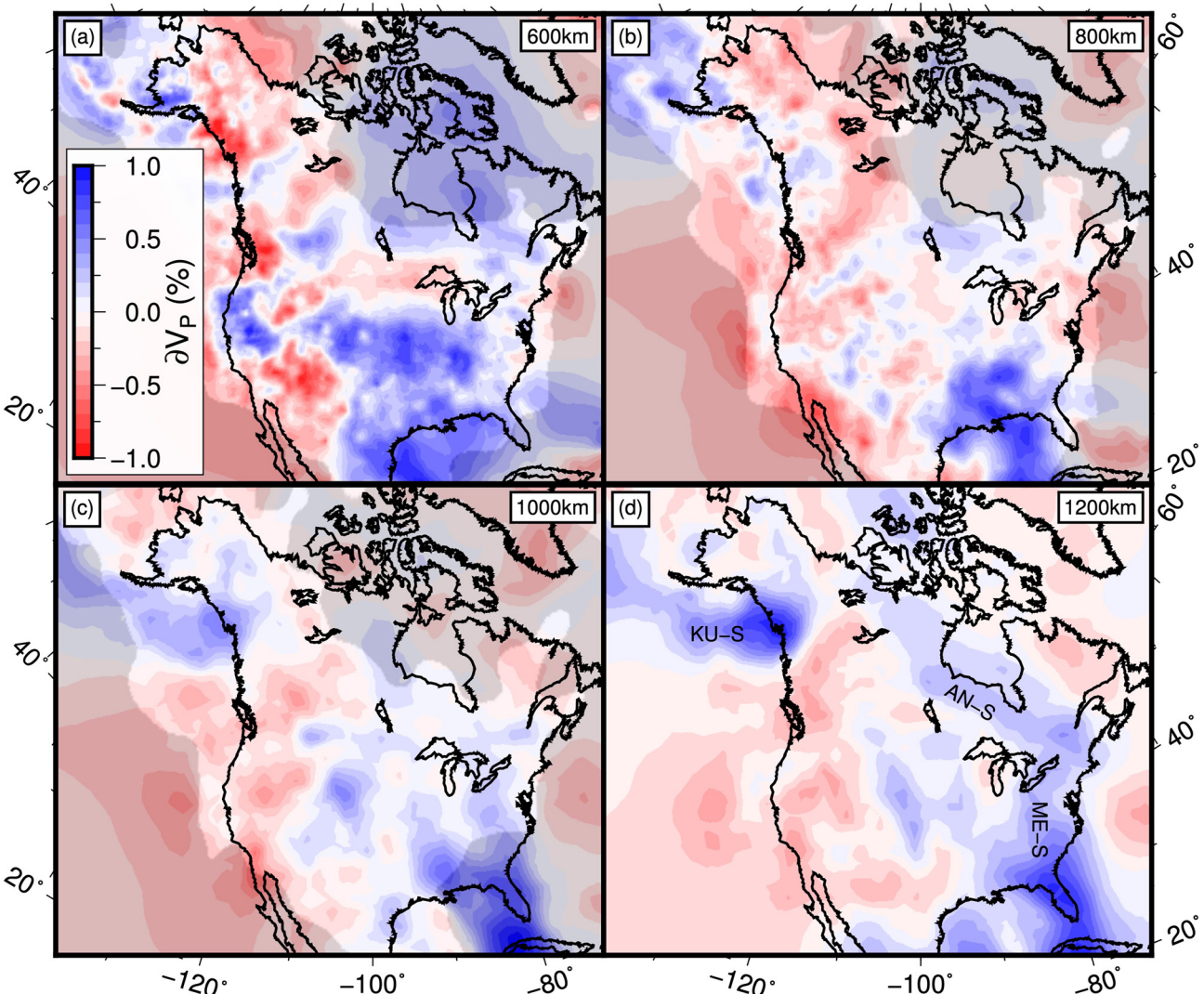


**Figure 8.** CAP22 tomographic model at mid mantle depths of 600–1,200 km (a–d), plotted as deviation from ak135. Gray regions are unresolved according to recovery of  $5^\circ$  checkerboard anomalies (following Burdick et al., 2014, See Section 2.3). KU-S: Kula slab, AN-S: Angayucham slab, ME-S: Mezcalera slab.

further inversions using only these data (Figure 12) using the same parameterization and regularization as the final model rather than optimizing inversion parameters in each case (Section 2.2). We also perform a resolution test using  $5^\circ$  checkerboards with each data set.

Recovery of the checkerboard test (Figure 12) shows that the contiguous US and Alaska are very well resolved by the “EHB-TA” data, but resolution decays abruptly north of the US-Canadian border. “CAP22-only” data are required to resolve wavespeeds in Canada, particularly below denser station coverage in the west and southeast. Without the “CAP22-only” data, the final inversion is unable to reliably image the upper mantle wavespeed transition that follows the RMT in southwest Canada and deviates inland beyond the CDF toward the Slave Craton in northwest Canada. Structural complexities within the arcuate fast wavespeed anomaly in southern Alaska are only revealed by the “EHB-TA” data, while the “CAP22-only” data captures smoother structure.

Despite the increased weighting given to CAP22 data, the “EHB-TA” data are likely to dominate the inversion below most of North America at mid-mantle depths (800–1,200 km). Interestingly, the “CAP22-only” data inversion reveals striking smooth fast wavespeed structures that are significantly more patchy within the “EHB-TA” and final inversions. At 800 km depth, a broad fast wavespeed anomaly ( $\delta V_p > 0.25\%$ ) stretches from Hudson Bay southward to the Gulf of Mexico indicating some flattening of a fast wavespeed anomaly at this depth. This wavespeed signature is incoherent when “EHB-TA” data are used. At greater depth (1,000–1,200 km) the

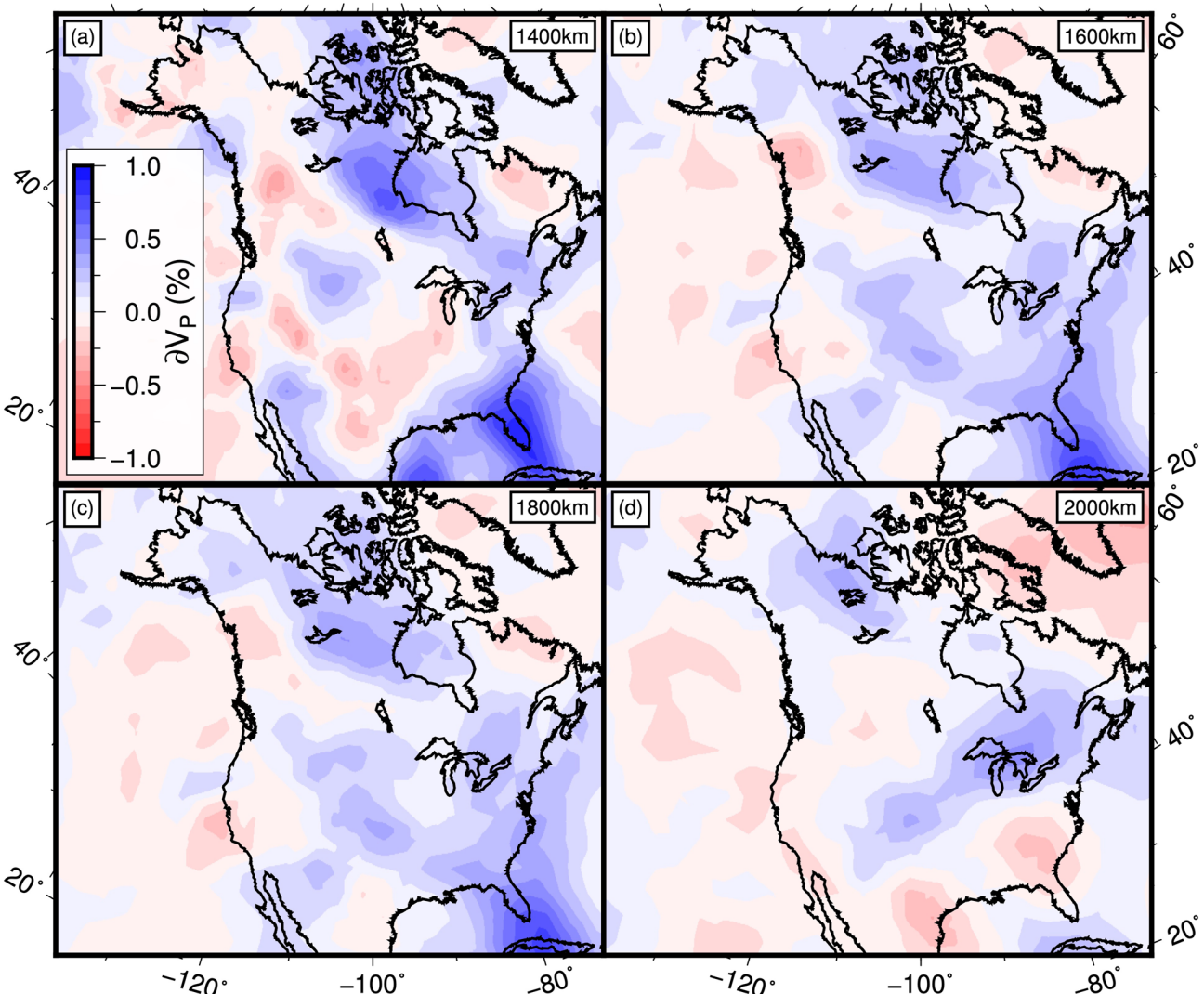


**Figure 9.** CAP22 tomographic model at lower mantle depths of 1,400–2,000 km (a–d), plotted as deviation from ak135.

fast wavespeed anomalies aligned north-south below eastern North America and aligned southeast-northwest centered below western Hudson Bay are substantially smoother when imaged with “CAP22-only” data compared to when including “EHB-TA” data. The southeast-northwest aligned anomaly is not well recovered by “EHB-TA” data alone. Finally both “EHB-TA” and “CAP22-only” data inversions reveal the fast wavespeed anomaly below southwest Yukon and offshore southern Alaska (1,000–1,200 km depth).

### 3.3. CAP22 Compared With Previous Studies

#### 3.3.1. Canada

Figure 13 compares CAP22 to four global P-wave models that capture wavespeed variation throughout North America: PRI-P05 (Montelli et al., 2006), MIT-P08 (C. Li, Van der Hilst, et al., 2008), LLNL-G3Dv3 (Simmons et al., 2012), DETOX-P2 (Hosseini et al., 2019). Within the contiguous US upper mantle, although amplitudes differ, the pattern of wavespeed variation is broadly similar across all models. Specifically, the location of the slow-to-fast wavespeed transition separating the active western US from the stable Precambrian interior shows good agreement. However, in Canada, substantial differences exist. Previous models do not show slow P-wavespeeds east of the CDF and beneath the Slave craton in northwest Canada, likely due to limited station coverage. Despite data differences, at  $\geq 1,000$  km depth CAP22 is largely similar to previous models (Figure 13).

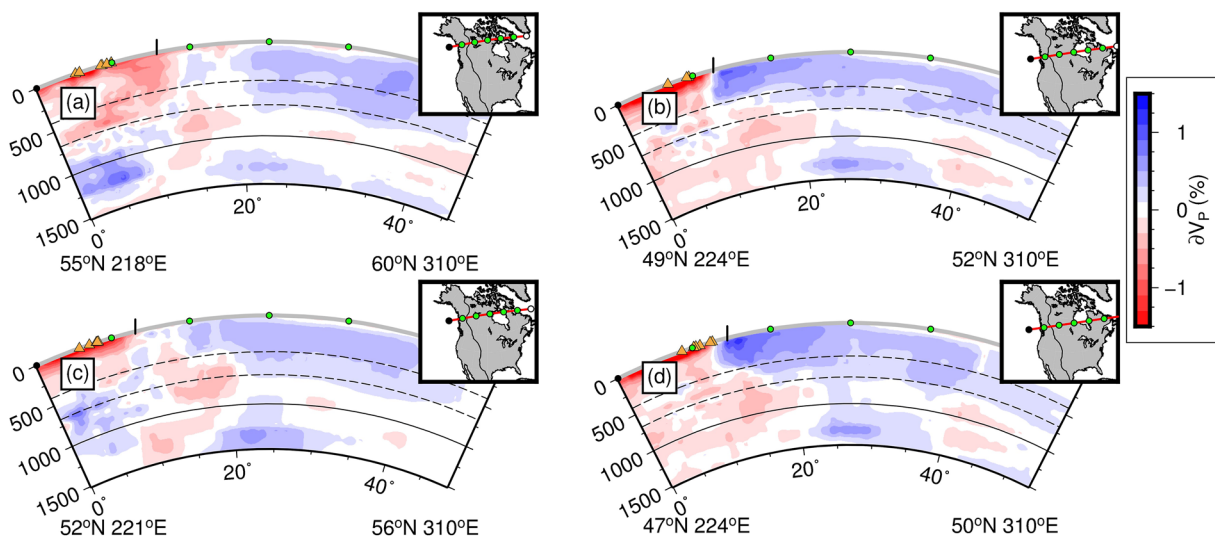


**Figure 10.** CAP22 tomographic model cross sections through Canada, plotted as deviation from ak135. Profiles traverse north-to-south (a, c, b, d). Orange triangles: locations of recent volcanism within  $1^{\circ}$  of the cross-section. Vertical black line at surface: location of CDF. Inset maps: cross section locations (red). CDF: black line.

Previous P-wave models using USArray TA data that focused on the contiguous US (e.g., Burdick et al., 2017; Schmandt & Lin, 2014) are similar to CAP22 at  $\leq 250$  km depth.

As far as we are aware, only the study of Boyce et al. (2019) has previously made a concerted attempt to address the drop in P-wavespeed resolution resulting from the termination of the USArray TA at or near the US-Canadian border, across which many significant geological boundaries traverse. Through improved resolution of the entire Grenville Province, evidence for higher wavespeeds at  $\leq 150$  km depth in the Proterozoic-and-older Canadian Grenville, compared to that in the younger US Grenvillian lithosphere farther south, was interpreted as variable subduction derived lithospheric modification modulated by the age/refractory nature of overlying lithosphere (Boyce et al., 2019). Likely resulting from improved crustal corrections prior to inversion and the balance of new data added here, CAP22 does not show this signature at  $\leq 150$  km depth, rather between 200 and 300 km depth, a result more easily explained by such a bottom-up process.

Narrow aperture regional body wave models of eastern Canada, often determined using relative arrival time analysis, are widely available for the northern Superior Province and Hudson Bay (e.g., Bastow et al., 2015; Liddell et al., 2018), southeastern Superior Province and coastal domains (e.g., Boyce et al., 2016; Villemaire et al., 2012) and western Superior Province (e.g., Frederiksen et al., 2013). CAP22 indicates that the highest P-wavespeed anomaly at lithospheric depths in Canada does not lie in the western Superior Province (Frederiksen et al., 2013), but rather southwestern Canada, just east of the CDF. CAP22 also shows wavespeeds decreasing progressively eastwards toward the coast through the Grenville into the Appalachian Province (Boyce et al., 2016), and evidence for locally decreased wavespeeds below the proposed track of the Great Meteor Hotspot track across these domains (Boyce et al., 2016; Villemaire et al., 2012). In contrast to Liddell et al. (2018), CAP22 shows slight variation in lithospheric wavespeeds between the Paleoarchean Rae and Mesoarchean Hearne domains. While the faster wavespeeds in the Rae domain could be associated with greater age compared to the Hearne (and therefore perhaps depletion levels), this observation may be influenced by poorer station coverage in northeastern Hearne domain, compared to the adjacent Rae craton.

Similar to eastern Canada, western Canada has been the subject of numerous regional body wave studies focused on continental lithospheric scale structures (e.g., Y. Chen et al., 2018, 2019; Estève et al., 2019, 2020; Frederiksen et al., 1998; Mercier et al., 2009), against which CAP22 can be compared. In western Canada, the position of the Cordillera-craton transition marked by a slow-to-fast wavespeed boundary has been the subject of significant debate, because its position and character have significant implications for Cordilleran formation hypotheses. In southwest Canada, the westward dip of the wavespeed boundary imaged below the RMT by Y. Chen et al. (2018, 2019) is thought to favor a collisional origin for the Cordillera, resulting from an accretion of an allochthonous ribbon microcontinent or archipelago to cratonic North America (e.g., Johnston, 2008; Sigloch

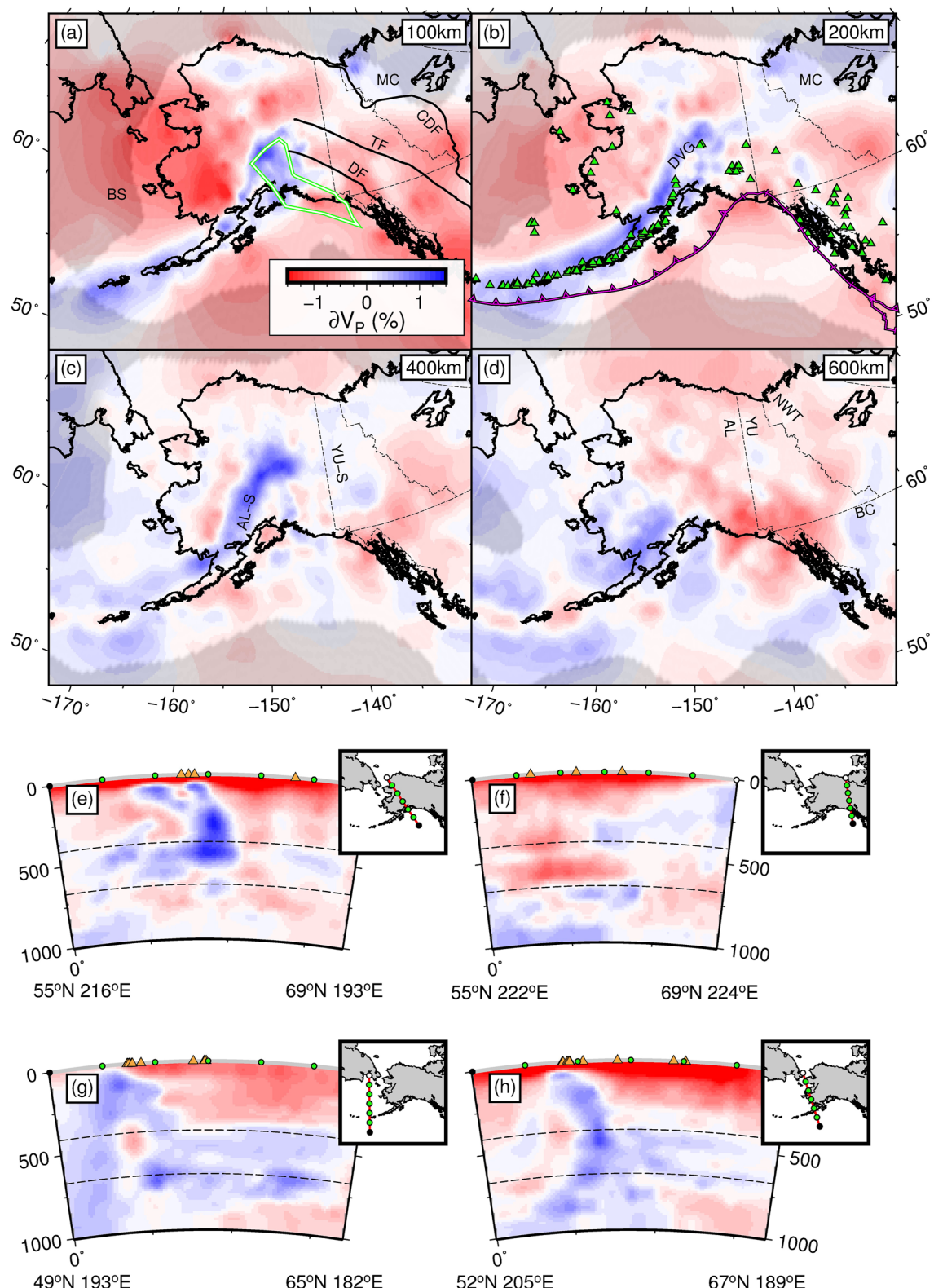


**Figure 11.** CAP22 tomographic model at several depths (100–600 km; a–d) and cross sections (e–h) for Alaska, plotted as deviation from ak135. Gray regions are unresolved according to recovery of  $5^\circ$  checkerboard anomalies (following Burdick et al., 2014, See Section 2.3). Yukat terrane: green outline (after Eberhart-Phillips et al., 2006). Quaternary volcanoes: green triangles. BS: Bering Sea, CDF: Cordilleran Deformation Front, DF: Denali Fault, DVG: Denali Volcanic Gap, MC: Possible location of Mackenzie Craton, TF: Tintina Fault. AL-S: Alaskan slab, YU-S: Yukon slab. Other structural and political boundaries as in Figure 1. Orange triangles: locations of recent volcanism within  $1^\circ$  of the cross-section.

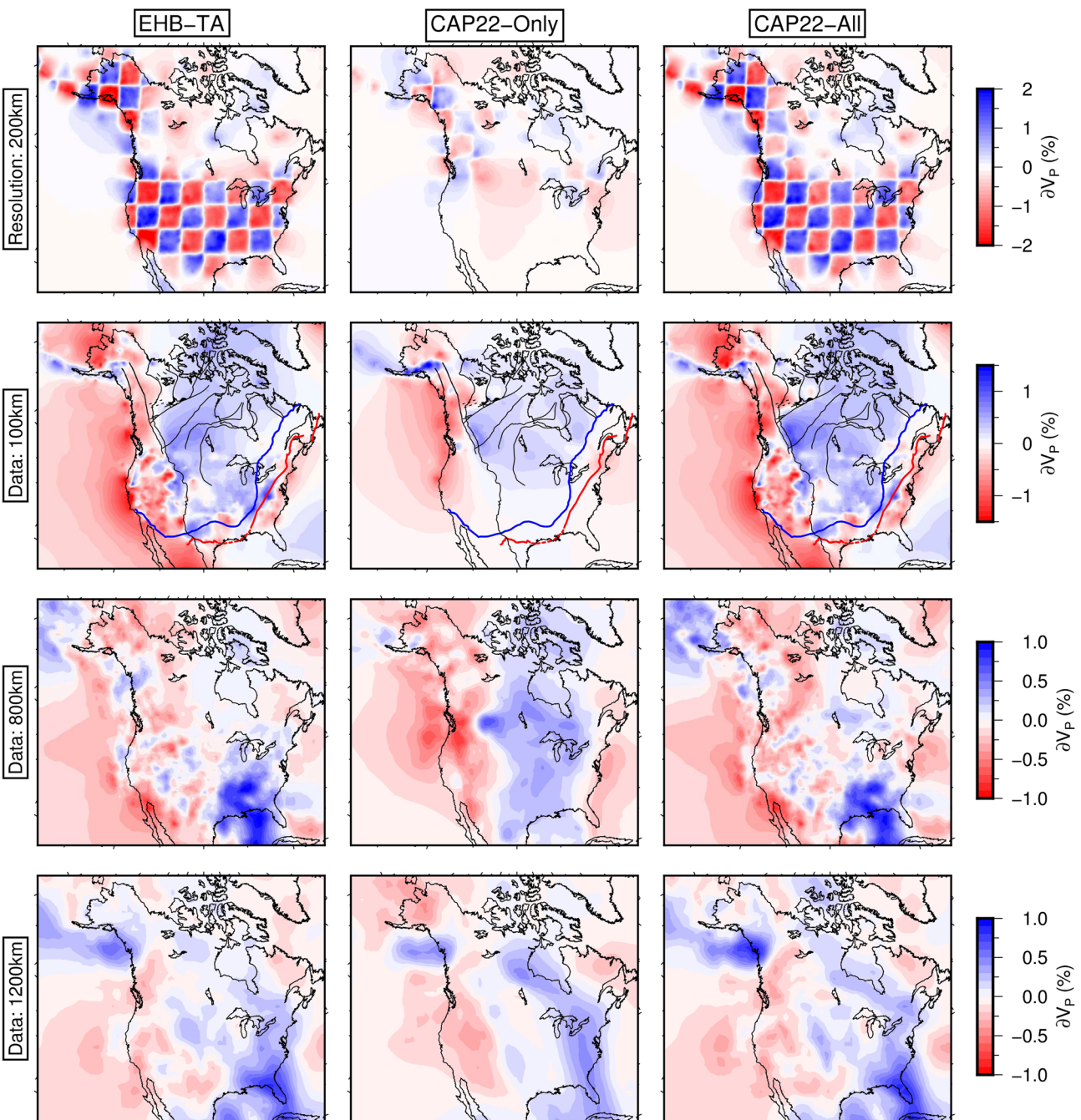


**Figure 12.** Influence of different data sets in CAP22 inversion. Left: Inversion using only global and USArray Transportable Array (EHB-TA) data. Middle: Inversion using only absolute arrival-times from SE Canada processed by Boyce et al. (2019) and new data processed here (CAP22-only). Right: Inversion using all data as in previous figures. All inversions were performed with identical parameterization and regularization. Top: Recovery of 5° degree checkerboard resolution test (e.g., Figure 3) at 200 km depth. Middle/Bottom: Output of data inversion from 100 to 1,200 km depth. Note variable velocity scale. Structural boundaries as in Figure 1.

& Mihalynuk, 2013). Steep westward dipping boundaries imaged at this location in CAP22 (Figure 10) directly corroborate this interpretation, however steep apparent westward dip in recovered anomaly boundaries within our structural resolution testing here (Figures 5l and 5p) means this result is somewhat uncertain. To the north, while Frederiksen et al. (1998) placed the boundary of Precambrian North American lithosphere west of the Tintina Fault and Mercier et al. (2009) suggest this boundary underlies the CDF in northwest Canada, more recent studies suggest that low wavespeeds continue beyond the CDF, east of the Mackenzie Mountains toward the Slave craton

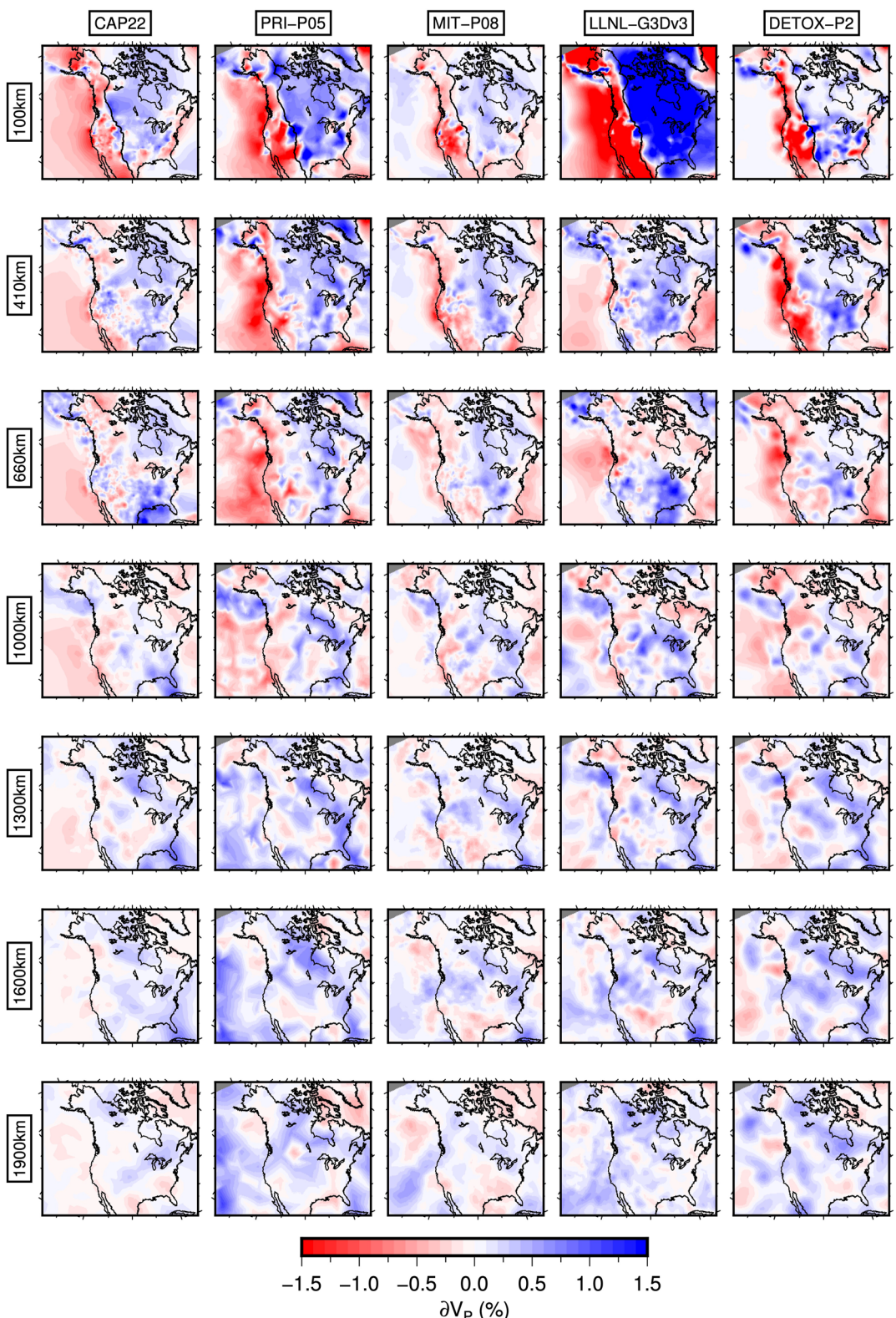


**Figure 13.** CAP22 tomographic model compared to four other global-scale P-wave tomographic models: PRI-P05 (Montelli et al., 2006), MIT-P08 (C. Li, Van der Hilst, et al., 2008), LLNL-G3Dv3 (Simmons et al., 2012), and DETOX-P2 (Hosseini et al., 2019). Models are plotted with respect to the reference model specific to each inversion. Black line: Cordilleran Deformation Front.

(Estève et al., 2019, 2020). CAP22 also shows slow wavespeeds to continue eastward throughout the Slave craton, with the abrupt change spatially correlated with the LLTZ. We return to this observation in Sections 4.4 and 4.5.

Moving outboard toward the coast in western Canada at the northern end of Vancouver Island, resolution is at best 1.5–2.0°. Thus, we are unable to confidently interpret wavespeed anomalies of length-scales associated with subducted fragments of the Explorer micro plate at ~52°N (e.g., Mercier et al., 2009). Therefore, fast wavespeeds easily linked to Cascadia subduction of the Gorda, Juan de Fuca and Explorer plate system, appear to terminate south of ~50°–51°N in CAP22 (Figures 6 and 7, e.g., Audet et al., 2008; Bostock & Vandecar, 1995; Savard et al., 2020). To the northwest, the transformation of the convergent plate boundary to predominately strike slip motion along the Queen Charlotte Fault (QCF: ≈50 mm/yr - see Figure 6; DeMets & Dixon, 1999; Mazzotti et al., 2003) also requires a component of oblique convergence (≈15–20 mm/yr). Some authors have suggested that deformation of the North American margin accommodates compression (e.g., Brothers et al., 2020; Rohr et al., 2000), while others propose partial underthrusting of the Pacific slab (e.g., Bustin et al., 2007; Gosselin et al., 2015; Hyndman, 2015; Lay et al., 2013; Smith et al., 2003; Yorath & Hyndman, 1983). Within resolution constraints, distinct isolated fast wavespeed fragments are visible between the QCF and western Canadian coastline at 200–400 km depth in CAP22 (Figure 7; similarly to Mercier et al., 2009) meaning that our model is perhaps in greater agreement with a hypothesis of fragmented subduction of the Pacific plate to accommodate convergence along the QCF. However, we are not able to resolve the dip of these features (e.g., Audet et al., 2008).

Cognizant of the differing data sensitivities and resolving power of tomographic models containing surface wave data and their P-wave counterparts, a comparison between them can offer useful insights into causes of seismological heterogeneity, especially where differences exist. Figure 14 compares CAP22 to three S-wave models at upper mantle depths: SL2014NA (Schaeffer & Lebedev, 2014), SEMum\_NA14 (Yuan et al., 2014), CAM2016Vsv (Priestley et al., 2019). Global models typically reveal a fast shear wavespeed cratonic core centered around central Canada and Hudson Bay with decreasing wavespeeds below the surrounding Proterozoic interior and slow wavespeeds below the western side of the continent in the upper mantle (e.g., Priestley et al., 2019; Ritsema et al., 2011). Due to increased resolving power offered by USArray TA data, continental-scale S-wave models (e.g., Schaeffer & Lebedev, 2014; Yuan et al., 2011; Yuan et al., 2014, see Figure 14) typically offer substantially improved resolution laterally, revealing correlations with surface geological boundaries. Fast shear wavespeeds in North America are confined to between the CDF and Appalachian Front at upper mantle depths with the most anomalous regions centered around central Canada. Outside of this, substantially slower wavespeeds are present. The slow-to-fast shear wavespeed boundary follows the CDF (Bao et al., 2014; Schaeffer & Lebedev, 2014; Yuan et al., 2014) throughout western Canada, tracing out the arcuate shape of the Mackenzie Mountains in the northwest. Overall in Canada, shear-wave models do not image significantly reduced wavespeeds continuing east of the CDF from the Mackenzie Mountains into the Slave craton bounded by the LLTZ in the south as seen in CAP22.

### 3.3.2. Alaska

In Alaska, CAP22 shows the arcuate shape of the fast wavespeed Alaskan slab and its termination following a sharp kink below south-central Alaska just east of the subducted Yakutat Terrane (Figures 11a–11c). This result agrees with the well-documented Wadati-Benioff zone (Page et al., 1991; Ratchkovski & Hansen, 2002) and previous tomographic studies (e.g., Burdick et al., 2017; Martin-Short et al., 2016). The break in imaged fast wavespeeds below the DVG separating two north-northwest dipping fast wavespeed anomalies below the Yakutat Terrane (Figures 11b and 11e) has not been clearly revealed in prior broad-scale tomographic studies that used less data than in CAP22 or reveal smoother heterogeneity (e.g., Burdick et al., 2017; Gou et al., 2019; Jiang et al., 2018; Martin-Short et al., 2016). However, this observation is consistent with a double layered structure beneath the DVG found in local earthquake tomography to ~150 km depth (Eberhart-Phillips et al., 2006; Nayak et al., 2020). This feature may be on the lower bound of our resolution however (Figure S24 in Supporting Information S1). Similarly to more recent models (e.g., Gou et al., 2019; Jiang et al., 2018), CAP22 displays evidence for fast wavespeeds continuing northeast of Yakutat Terrane on the Alaskan slab and below the WVF at ~100–200 km depth, a feature less clear in earlier models (e.g., Martin-Short et al., 2016, 2018; Qi et al., 2007; Wang & Tape, 2014). At greater depths the flattening of the Alaskan slab in the mantle transition zone below western Alaska (Figures 11d, 11g and 11h) agrees with previous results (e.g., Burdick et al., 2017; Qi et al., 2007; Zhao et al., 2010). Although resolution in CAP22 decays toward the west (e.g., Figure 4 and Figure S23 in Supporting Information S1), below western Alaska and the Bering Sea, broad slow wavespeeds overly the stagnant Pacific slab at ≤400 km depth (Figures 11g and 11h). This means CAP22 could be used to argue for a

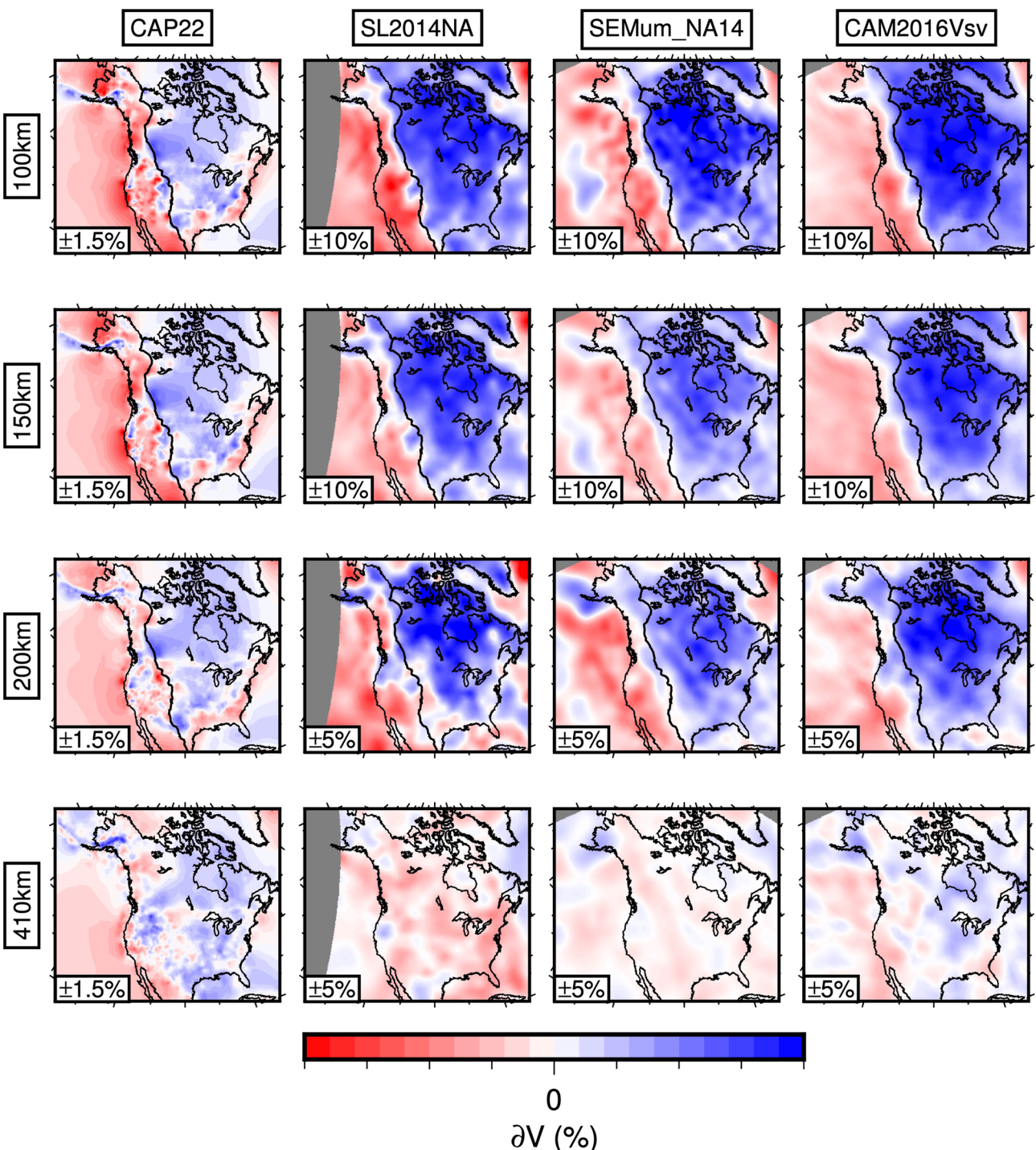


**Figure 14.** CAP22 tomographic model compared to three S-wave tomographic models: SL2014NA (Schaeffer & Lebedev, 2014), SEMum\_NA14 (Yuan et al., 2014), CAM2016Vsv (Priestley et al., 2019). Models are plotted with respect to the reference model specific to each inversion. Wavespeed deviation shown in lower-left corner of each sub-figure. Black line: Cordilleran Deformation Front.

hypothesis of intraplate volcanism in the region resulting from dehydration of the deep, stagnant Pacific slab (e.g., Zhao et al., 2009; Zhao et al., 2010).

Based on published P-wave tomography models, Fuston and Wu (2021) mapped a fast wavespeed anomaly below northeast Alaska and northwest Yukon at  $\sim 200\text{--}500$  km depth but this feature likely resides at the edge of prior

data coverage. CAP22 reveals this “Yukon slab” at  $\sim$ 200–400 km (Figures 11c and 11f) by capitalizing on overlying stations meaning this feature should be robustly resolved (Figure 4 and S23 in Supporting Information S1). Finally, the deep fast wavespeed anomaly offshore southern Alaska and western British Columbia at 600–1,200 km depth (often called “Kula slab” e.g., Clennett et al., 2020) terminates 100 km shallower in depth than previously observed (Figures 8 and 13; also see Hosseini et al., 2019; C. Li, Van der Hilst, et al., 2008; Montelli et al., 2006; Simmons et al., 2012). This indicates less vertical smearing in CAP22 compared to previous models.

## 4. Discussion

### 4.1. Evidence for Fast Velocities Beneath the Wrangell Volcanic Field

The causal mechanism for the WVF at the eastern edge of the Yakutat Terrane on the subducting Alaskan slab has, until recently, been a topic of controversial debate (e.g., Jadamec & Billen, 2010; Martin-Short et al., 2016). CAP22 shows evidence for fast wavespeed material at  $\sim$ 100–200 km depth below the WVF, northeast of the fast velocities below the subducting Yakutat terrane (Figure 11).

Some previous tomographic studies (e.g., Martin-Short et al., 2016; Nayak et al., 2020) show no evidence for fast velocities below the WVF, while shear wave splitting measurements often show complex patterns of seismic anisotropy in the region (e.g., Christensen & Abbers, 2010; McPherson et al., 2020; Venereau et al., 2019; Yang et al., 2021), leading to a variety of exotic mechanisms to produce the WVF (e.g., toroidal flow around a slab edge; Jadamec & Billen, 2010). However, some recent tomographic images display evidence for fast upper mantle wavespeeds near the WVF (e.g., Gou et al., 2019; Jiang et al., 2018), likely corresponding to emerging evidence for a dipping Wadati-Benioff zone beneath the Wrangell volcanoes to  $\sim$ 100 km depth (Daly et al., 2021), a dipping fast velocity structure (Mann et al., 2022) and mantle wedge structure revealed by seismic attenuation (Castaneda et al., 2021).

The fast upper mantle wavespeeds below the WVF in CAP22 continuing east of the Yakutat Terrane favor a conventional subduction related mechanism for WVF (Daly et al., 2021; Mann et al., 2022). While CAP22 shows good agreement with the newly proposed outline for the slab beneath the WVF (Daly et al., 2021; Mann et al., 2022), our images do not show any convincing evidence for a slab tear (Daly et al., 2021; Jiang et al., 2018; Mann et al., 2022) separating fast wavespeed material beneath the WVF and below the adjacent Yakutat/Alaskan slab. Although lateral resolution here is good (e.g., Figure S24 in Supporting Information S1), such a slab tear may be below the limit of our resolution.

### 4.2. Evidence for the Mackenzie Craton

Under the thick sedimentary cover in northwest Canada, previous studies have suggested the presence of an unexposed Mackenzie craton around the northern Yukon-NWT border, east of the CDF (e.g., Estève et al., 2020; Schaeffer & Lebedev, 2014). Imaging of this region is hindered by a gap in station coverage between the eastern extent of the USArray TA in Yukon and the Mackenzie Mountain Transect (Baker et al., 2020). Available stations (Figure 2) show early absolute arrival-times ( $-0.5$  to  $-0.25$  s) that are less anomalous than within cratonic regions elsewhere ( $\leq -1.0$  s). However, resolution testing (Figures 3 and 4) indicates that fast upper mantle wavespeeds of lateral extent  $\sim$ 3–5° should be resolvable there in CAP22. Indeed, CAP22 reveals a fast wavespeed anomaly ( $\delta V_p \approx 0.3\%$ , 100–300 km depth) northeast of the Yukon-NWT border and CDF (MC: Figures 6 and 11).

Based on a very similar station distribution to CAP22, Estève et al. (2020) used relative arrival-time data to image high P- and S-wavespeeds below the proposed Mackenzie craton, with elevated wavespeeds continuing west of the CDF. Surface wave tomography (Schaeffer & Lebedev, 2014), capable of resolving wavespeed variations between stations, shows fast wavespeeds east of the CDF in this region, which provides strong evidence in favor of the Mackenzie craton. Other geophysical observables such as the strong, deep magnetic high imaged in this region (Saltus & Hudson, 2007), provide further evidence for the presence of the Mackenzie craton. Despite limited station coverage, CAP22 provides reasonable evidence for a Mackenzie craton, although new station deployments are required in the region to confirm its lateral extent using body waves.

### 4.3. Evidence for the Yukon Slab: Consequences for Western North America Subduction History

Plate tectonic reconstructions can be better constrained by considering subducted remnants in the mantle (e.g., Clennett et al., 2020; Domeier et al., 2017; Fuston & Wu, 2021; Sigloch & Mihalynuk, 2013), meaning CAP22

offers new insights into contentious debate concerning the building of western North America as the Laurentian core drifted westwards since Mesozoic times (e.g., Clennett et al., 2020; Engebretson et al., 1985; Fuston & Wu, 2021; Müller et al., 2019; Sigloch & Mihalynuk, 2013). At mid-to-lower mantle depths ( $\sim$ 1,200–2,000 km), CAP22 resolves the north-south striking Mezcalera and northwest-southeast striking Angayucham slabs (ME-S; AN-S Figures 5, 8 and 9; e.g., Sigloch & Mihalynuk, 2013) as broad fast wavespeed features. Consequently, rather than favoring traditional plate reconstructions that propose approximately continuous eastward subduction below western North America during Mesozoic times (e.g., Engebretson et al., 1985; Müller et al., 2019), CAP22 better supports westward oceanic subduction below a ribbon continent or archipelago during the Mesozoic ahead of westward drifting North America (e.g., Clennett et al., 2020; Johnston, 2001, 2008; Sigloch & Mihalynuk, 2017). This alternative model is often considered more favorable alongside paleomagnetically constrained northward translation of Alaskan terranes for  $>$ 2,000 km (e.g., Beck & Noson, 1972; Johnston, 2001), resulting in terminal formation of Alaska at  $\sim$ 50 Ma.

At shallower depths ( $\sim$ 400–1,200 km), several fast wavespeed anomalies have been variably interpreted to constrain the more recent subduction history of western North America ( $\leq$ 80 Ma, e.g., Clennett et al., 2020; Fuston & Wu, 2021). Fast wavespeeds in CAP22 and previous studies at mid-mantle depths offshore southern Alaska (KU-S, 1,000–1,200 km, Figures 8c and 8d, 13) prompt reconstructions to at least partially subduct the Kula plate northwards offshore, in a relative position southward of the modern Alaskan subduction zone. The latter was established after offshore Kula subduction ceased (Clennett et al., 2020). Termination of offshore Kula subduction coevally terminates the northward subduction of the smaller “Resurrection” or “Orcas” plate at  $\sim$ 47 Ma, which separates the Kula and Farallon plates. However, Clennett et al. (2020) do not focus attention on remnants of the Resurrection/Orcas plate in the mantle following subduction termination, some of which may be present below northwest Yukon (Fuston & Wu, 2021).

One region of improved resolution in CAP22 over previous P-wave models, such MIT-P08 and MIT-P16 (Burdick et al., 2017; C. Li, Van der Hilst, et al., 2008) used in the reconstructions of Fuston and Wu (2021), is northern Yukon and northwestern-most NWT. Here, CAP22 shows evidence for a  $\delta V_p \approx 0.2$ –0.3% fast wavespeed anomaly at 400 km depth (YU-S; Figure 11c) separated from the Alaskan slab (AL-S; Figure 11c). This feature is not likely associated with the Mackenzie craton because much of this anomaly lies southwest of the CDF and YU/NWT provincial border at 400 km depth. Our model therefore provides further support for a shallow slab remnant below this region, termed the “Yukon Slab” by Fuston and Wu (2021), as a possible remnant of Resurrection/Orcas subduction.

Fuston and Wu (2021) state that tomographic and magmatic evidence for the Yukon slab is more easily explained by the consistent subduction of three plates (and two separating ridges) below the North American continental margin and no more than 1,200 km of terrane translation, rather than by a model of Kula/Orcas ridge subduction below an intra-oceanic subduction zone southwest of modern Alaska (e.g., Clennett et al., 2020, see Figure 15 for schematic comparison). However, the model of Fuston and Wu (2021), which lacks offshore subduction of the Kula plate outboard of the modern Alaska/Aleutian Arc, means the fast wavespeed anomaly at 800–1,200 km offshore southern Alaska in prior models and CAP22 (Figures 8c and 8d, 13), is unexplained and consequently ignored by these authors. Therefore, the most recent tomographic evidence from CAP22, constraining both the Kula slab in the mid mantle and the Yukon slab at shallower depths, is not entirely consistent with existing plate reconstructions for western North America subduction history (e.g., Clennett et al., 2020; Fuston & Wu, 2021; Müller et al., 2019). With the likelihood of future studies revealing greater evidence for the Yukon slab, it therefore appears that further improvements to plate reconstructions are required to reconcile these new observations.

#### 4.4. Metasomatic Modification of the Slave Craton

Fundamental constraints on the spatial distribution of Slave craton modification are lacking because geological studies have often focused on spatially limited xenolith samples (Aulbach et al., 2013; Heaman & Pearson, 2010) and 3D geophysical studies have been limited to long wavelength surface wave models (e.g., Schaeffer & Lebedev, 2014) and relative arrival time models that are unable to capture the background mean (e.g., Bank et al., 2000; Estève et al., 2019, 2020). New measurements (Figure 2) reveal delayed arrivals northeast of the CDF in the southern Mackenzie Mountains ( $\sim$ 0.5–1 s) throughout much of the Proterozoic arcs and into the central Archean Slave craton. To the south, the GSLsz and LLTZ coincide with the transition to predominantly fast residuals east of the CDF.

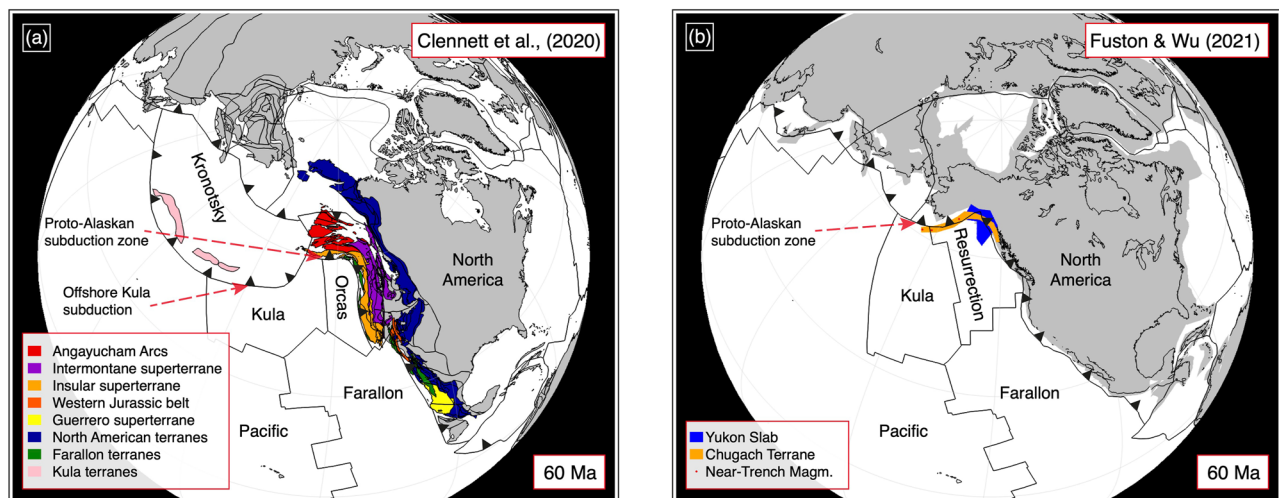


**Figure 15.** Plate tectonic reconstructions at  $\sim 60$  Ma plotted using GPlates (<https://www.gplates.org/>, Müller et al., 2018) adapted from (a) Clennett et al. (2020) and (b) Fuston and Wu (2021). Geological terranes important to each reconstruction shown in lower left. Major plates are labeled. Notable subduction zones are indicated with dashed red arrows.

Similarly to the distribution of residuals, CAP22 shows the highest amplitude, slow wavespeed anomalies in the northwest Canadian upper mantle are focused below the Cordillera and southern Mackenzie Mountains and Proterozoic arcs eastwards of the CDF ( $\delta V_p < -1.4\%$ , Figure 7). To the east, the Slave craton shows peak slow wavespeed amplitudes of  $\delta V_p \approx -0.3\%$  at 100 km depth that decay at greater depth toward the global mean (200–300 km depth). Schaeffer and Lebedev (2014) noticed that most diamondiferous kimberlites throughout North America are located on the edge, or within regions of fast craton-like shear wavespeeds at lithospheric depths. However, in CAP22, central Slave craton kimberlites are underlain by slow upper mantle compressional wavespeeds in contrast to those elsewhere across the continent (Figure 6). This observation therefore motivates an explanation for the physical state of the Slave craton mantle that affects P-wavespeeds to a greater extent than their S-wave counterparts (i.e., lowered  $V_p/V_s$  ratio).

The impact of post formation metasomatism has been discussed at length to both explain geophysical (C.-W. Chen et al., 2009; Eeken et al., 2018; Estève et al., 2019) and geochemical observations (Aulbach et al., 2007, 2013; Griffin et al., 2003, 2004; Heaman & Pearson, 2010; Liu et al., 2021; Pearson & Wittig, 2008; Tomlinson & Kamber, 2021; Veglio et al., 2022) of the Slave craton. Previous workers have often favored a layered structure for the Slave craton with a boundary at 100–150 km depth between lithosphere of different regimes (Griffin et al., 2004; C.-W. Chen et al., 2009; Veglio et al., 2022). However, there is contention regarding the layer(s) in which significant metasomatism is observed and by which mechanisms (e.g., Aulbach et al., 2013; Eeken et al., 2018; Griffin et al., 2003, 2004). Pearson and Wittig (2008); Heaman and Pearson (2010); Tomlinson and Kamber (2021) and others suggest that an enrichment in orthopyroxene through the addition of silica to the lithospheric mantle in a subduction related process provides an adequate mechanism to explain the metasomatic enrichment whilst other authors prefer the addition of other minerals such as phlogopite, antigorite, graphite and carbonatite (e.g., C.-W. Chen et al., 2009; Eeken et al., 2018; Veglio et al., 2022).

To explain the striking difference in P-wavespeeds below the central Slave craton and western Proterozoic terranes compared to existing S-wave models (e.g., Schaeffer & Lebedev, 2014; Yuan et al., 2014, see Figure 14), we consider the addition of orthopyroxene to the continental upper mantle (e.g., Kelemen et al., 1998), because to our knowledge it is the only form of metasomatism that has been shown to result in a measurable ( $\sim 1.0\%$ ) reduction in P-wavespeed, while S-wavespeeds and density remain relatively unchanged (Schutt & Lesher, 2010; Wagner et al., 2008). Here, melt/rock interaction in the overlying plate leads to the addition of silica through the production of orthopyroxene. Previous authors have suggested that the Slave craton formed the upper plate in the Wopmay orogen, which resulted in the accretion of Proterozoic terranes to the west (Hoffman, 1988; Schmidberger et al., 2007). Consequently, subduction is thought to be the most effective to produce a metasomatic signature in Late-Archean-Early Proterozoic times (Pearson & Wittig, 2008; Tomlinson & Kamber, 2021) because the Mackenzie Plume is thought to only have interacted with the northern Slave craton (Heaman &

Pearson, 2010; Liu et al., 2021). We therefore suggest that slow P-wavespeeds underlying the central Slave craton and westerly Proterozoic terranes, reflecting metasomatic modification by orthopyroxene enrichment due to ancient subduction, can account for the difference between CAP22 and previous S-wavespeed images.

#### 4.5. Evidence for Lithospheric Transfer Zones; Implications for Morphology of the Canadian Cordillera

In western Canada the morphology of the Cordillera (CCD) changes north-south along its length. The northern CCD is wide, bounded by an arcuate CDF, while the southern CCD is relatively narrow, bounded by a linear CDF, approximately parallel to the coastline. The geomorphological change in the CCD is often linked to the Liard Line Transfer Zone (LLTZ) north of the Macdonald Hay-River fault, which is the surface expression of the Great Slave Lake shear zone (GSLsz; Cecile et al., 1997; Hayward, 2015; Hayward & Paradis, 2021; Lund, 2008; see Figure 1). Geologically, the LLLTZ is interpreted as the boundary between two asymmetric rifting modes along the western margin of Laurentia (e.g., Cecile et al., 1997; Lister et al., 1986; Lund, 2008). North of the LLLTZ, a “lower-plate” type rifted margin is interpreted, consistent with the wide sedimentary basins (Lund, 2008) and thinner crust (Audet et al., 2020). To the south of the LLLTZ, the narrow expression of the Cordillera and thicker crust is consistent with an “upper-plate” type margin. The LLLTZ has also been associated with a change in mineral deposit distribution (Lund, 2008), earthquake distribution and anisotropic fabrics (Audet et al., 2016), mantle xenolith composition (Hayward, 2015) and a southwards crustal thickening (Audet et al., 2020; Clowes et al., 2005), yet links to variations in the lithospheric mantle wavespeeds have remained somewhat tentative (Estève et al., 2020).

In CAP22, upper mantle slow wavespeeds below the southern CCD are separated from fast wavespeeds of the Precambrian interior by a steep westward dipping boundary below the RMT. By contrast, slow wavespeeds below the northern CCD continue northeastward of the Mackenzie Mountains beyond the CDF into the central Slave craton (Figures 6–10). This north-south change in wavespeed pattern is colocated with the change in geomorphic expression along the CCD, and importantly the LLLTZ, implying that such transfer zones are not limited to crustal depths.

In northwest Canada, magnetic anomaly data resolve high-amplitude magnetic highs bounding the Mackenzie Mountains to the north and south (Saltus & Hudson, 2007), interpreted as mafic lower crust and underlying depleted upper mantle. These inferred strong lithospheric blocks may provide buttresses to orogenic deformation and allow the CDF to develop its arcuate shape by broadening the northern CCD relative to its southern counterpart. Cordilleran deformation proceeded further eastward here because the Precambrian lithosphere to the east has been weakened through metasomatic modification (Section 4.4). In the south, the un-modified, depleted, fast wavespeed Laurentian lithosphere provides a strong backstop to deformation and limits the width of Cordilleran lithosphere. This is broadly consistent with inferences from ambient noise tomography from the Mackenzie Mountains indicating low lithospheric S-wavespeeds, and inferred rheological weakness, beneath the active Mackenzie thrust (Schutt et al., 2023), and its buttressing to the north and south by higher velocity and inferred stronger lithosphere (Estève et al., 2020). Together, these observations suggest that both tectonic inheritance from asymmetric rifting (Thomas, 2006) and lithospheric mantle strength variations control orogenic styles along the CCD.

### 5. Conclusions

We present CAP22, a new absolute P-wavespeed North American tomographic model. We combine global and continental-scale pick databases with >186,000 new hand picked measurements of absolute arrival-times from available temporary seismograph stations across Canada and Alaska, yielding the best station coverage yet achieved in this region specifically. The distribution of absolute arrival-time residuals broadly follows surface tectonics except in northwest Canada where delayed arrivals continue eastwards of the southern Mackenzie Mountains toward the central Slave craton. This differs from southwest Canada where delayed residuals are largely confined to within the Cordillera. The continuation of fast upper mantle wavespeeds below the WVF favors a conventional subduction related mechanism for volcanism. Although our model possesses imperfect resolution, CAP22 shows tantalizing evidence for the Mackenzie craton below the northern Yukon-NWT border. Seismic evidence for the subducted remnants of the Kula slab at mid-mantle depths offshore southern Alaska and fast wavespeeds centered at 400 km depth below NW Yukon and NWT (revealed by the latest USArray TA

deployment) are difficult to reconcile with competing tectonic reconstructions of western North America, meaning existing plate models may require revision. Slow P-wavespeeds terminate abruptly at the Rocky Mountain Trench in southwest Canada but continue landward beyond the Cordilleran Deformation Front into the central Slave craton, north of the Liard Line Transfer Zone. This is best explained by Archean-Proterozoic age subduction driven metasomatism of Precambrian Laurentian terranes, east of the present day Mackenzie Mountains, which can account for the observed difference between CAP22 and published S-wave models in this region. The imaged abrupt change in P-wavespeed coinciding with the Liard Line Transfer Zone inherited from prior tectonic regimes suggests that both the crust and mantle control changes in along-strike orogenic style in the Canadian Cordillera.

## Data Availability Statement

Phase arrivals from the EHB Bulletin are available at <http://www.isc.ac.uk/ehbulletin/>. Phase arrivals from USArray are available to the community as CSS monthly files from the ANF (<http://anf.ucsd.edu/tools/events/>). Seismic data was obtained (last accessed 06 Jul 2022) from the IRIS (<https://ds.iris.edu/ds/nodes/dmc/>) database and Canadian National Data Centre (<https://earthquakescanada.nrcan.gc.ca/stndon/CNDC/index-en.php>).

The waveform data used in each sub-region of this study during data processing are from the following networks: ALO: XO-2018 (Abers et al., 2018; Barchek et al., 2020). ALS: AK-1987 (Alaska Earthquake Center, Univ. of Alaska Fairbanks, 1987; D'Alessandro & Ruppert, 2012), AT-1967 (NOAA National Oceanic and Atmospheric Administration (USA), 1967; Oppenheimer et al., 2005), AV-1988 (Alaska Volcano Observatory/USGS, 1988; Dixon et al., 2013), GM-2016 (U.S. Geological Survey, 2016; Ringler et al., 2021), II-1986 (Ringler et al., 2021; Scripps Institution of Oceanography, 1986), IM-1965 (Ringler et al., 2021; Various Authors, 1965), IU-2014 (Albuquerque Seismological Laboratory/USGS, 2014; Ringler et al., 2021), PN-1998 (Indiana University Bloomington (IU Bloomington), 1998), US-1990 (Albuquerque Seismological Laboratory (ASL)/USGS, 1990; Ringler et al., 2021), XM-2011 (Keranen, 2011), XR-2004 (Song & Christensen, 2004), XV-2007 (Larsen & Truffer, 2007), XZ-2005 (Berger et al., 2008; Hansen & Pavlis, 2005), ZE-2015 (Tape et al., 2015, 2017). ALV: AV-1988 (Alaska Volcano Observatory/USGS, 1988; Dixon et al., 2013). HSB: CN-1975 (Natural Resources Canada (NRCCAN Canada), 1975; North, 1994; Bent et al., 2019), PO-2000 (Eaton et al., 2004; Geological Survey of Canada, 2000; Snyder et al., 2003), X5-2007 (University of Bristol (UK), 2007; Bastow et al., 2015). NWC: CN-1975 (Natural Resources Canada (NRCCAN Canada), 1975; North, 1994; Bent et al., 2019), NY-2013 (University of Ottawa (uOttawa Canada), 2013; Estève et al., 2020), PO-2000 (Eaton et al., 2004; Geological Survey of Canada, 2000; Snyder et al., 2003), RV-2013 (Alberta Geological Survey / Alberta Energy Regulator, 2013; Schultz et al., 2015), XN-2003 (Gaherty & Revenaugh, 2003; Mercier et al., 2009), Y5-2006 (University of Alberta (UAlberta Canada), 2006; Gu et al., 2011), YO-2016 (Yukon Geological Survey, 2016; Estève et al., 2019), 7C-2015 (Baker et al., 2020; Schutt & Aster, 2015). SWC: 1E–2018 (Natural Resources Canada (NRCCAN Canada), 2018; Babaie Mahani et al., 2019), 2K-2014 (Schultz et al., 2014, 2020), AK-1987 (Alaska Earthquake Center, Univ. of Alaska Fairbanks, 1987; D'Alessandro & Ruppert, 2012), C8-2002 (Natural Resources Canada (NRCCAN Canada), 2002), CN-1975 (Natural Resources Canada (NRCCAN Canada), 1975; North, 1994; Bent et al., 2019), EO-2018 (University of Calgary (U of C Canada), 2018; Boggs et al., 2018), PO-2000 (Eaton et al., 2004; Geological Survey of Canada, 2000; Snyder et al., 2003), RV-2013 (Alberta Geological Survey / Alberta Energy Regulator, 2013; Schultz et al., 2015), TD-2013 (TransAlta Corporation, 2013; Cui & Atkinson, 2016), XL-2017 (McGill University (Canada), 2017; Roth et al., 2020), XN-2003 (Gaherty & Revenaugh, 2003; Mercier et al., 2009), XY-2005 (Calkins et al., 2010; Dueker & Zandt, 2005), Y5-2006 (University of Alberta (UAlberta Canada), 2006; Gu et al., 2011). WUO (see Toomey et al., 2014): 7A-2010 (Woods Hole Oceanographic Institution (WHOI), 2010), 7D-2011 (IRIS OBSIP, 2011), OO-2013 (Rutgers University, 2013), X9-2012 (Nabelek & Braunmiller, 2012), Z5-2013 (Nabelek & Braunmiller, 2013).

Seismic data was subsequently processed using IRIS products, ObspyDMT (Hosseini & Sigloch, 2017) and GNU parallel (Tange, 2020). AARM is available as an electronic supplement to Boyce et al. (2017) or by contacting the corresponding author. Figures were plotted using Generic Mapping Tools (<https://www.generic-mapping-tools.org/>). A digital model file of CAP22 is available at <https://doi.org/10.17611/dp/emc.2023.cap22.1>. The raw data files, processed data, inversion software package and plotting codes are available under the doi: <https://doi.org/10.5281/zenodo.7510591>.

## Acknowledgments

This work was supported by the Natural Environment Research Council [NERC Grant reference number NE/R010862/1] and the European Research Council (ERC) under the European Union's Horizon 2020 research and innovation program (Grant agreement No. 804071 - ZoomDeep). Further support was provided by the West Hudson Bay Architecture and Metallogeny project of the GeoNorth program, Geological Survey of Canada. The facilities of EarthScope Consortium were used for access to waveforms, related metadata, and/or derived products used in this study. These services are funded through the Seismological Facility for the Advancement of Geoscience (SAGE) Award of the National Science Foundation under Cooperative Support Agreement EAR-1851048. Physiographic provinces in Figure 1 courtesy of V. M. Fernandes, M. Arnould and G. Pavlis are thanked for helpful discussions. We thank the editor and two reviewers for thoughtful comments that helped clarify the manuscript to aid reproducibility of results, and encouraged us to broaden the scope of our interpretations.

## References

- Abers, G., Wiens, D., Schwartz, S., Sheehan, A., Shillington, D., Worthington, L., et al. (2018). ACSE: Alaska amphibious community seismic experiment [Dataset] (seismic network). [https://doi.org/10.7914/SN/XO\\_2018](https://doi.org/10.7914/SN/XO_2018). International Federation of Digital Seismograph Networks
- Alaska Earthquake Center, Univ. of Alaska Fairbanks. (1987). Alaska regional network [Dataset] (seismic network). International Federation of Digital Seismograph Networks, <https://doi.org/10.7914/SN/AK> Retrieved from <https://www.fdsn.org/networks/detail/AK/>
- Alaska Volcano Observatory/USGS. (1988). Alaska Volcano Observatory [Dataset] (seismic network). Retrieved from <https://www.fdsn.org/networks/detail/AVI>. International Federation of Digital Seismograph Networks <https://doi.org/10.7914/SN/AV>
- Alberta Geological Survey / Alberta Energy Regulator. (2013). Regional Alberta observatory for earthquake studies network [Dataset]. International Federation of Digital Seismograph Networks. Retrieved from <https://www.fdsn.org/networks/detail/RV/> (Seismic Network) <https://doi.org/10.7914/SN/RV>
- Albuquerque Seismological Laboratory (Asl)/, USGS. (1990). United States National seismic network [Dataset] (seismic network). International Federation of Digital Seismograph Networks, <https://doi.org/10.7914/SN/US> Retrieved from <https://www.fdsn.org/networks/detail/US/>
- Albuquerque Seismological Laboratory/USGS. (2014). Global seismograph network (GSN - IRIS/USGS) [Dataset] (Seismic Network). International Federation of Digital Seismograph Networks, <https://doi.org/10.7914/SN/IU> Retrieved from <https://www.fdsn.org/networks/detail/IU/>
- Astiz, L., Eakins, J. A., Martynov, V. G., Cox, T. A., Tytell, J., Reyes, J. C., et al. (2014). The array network facility seismic bulletin: Products and an unbiased view of United States seismicity. *Seismological Research Letters*, 85(3), 576–593. <https://doi.org/10.1785/0220130141>
- Audet, P., Bostock, M. G., Mercier, J.-P., & Cassidy, J. F. (2008). Morphology of the explorer-Juan de Fuca slab edge in northern Cascadia: Imaging plate capture at a ridge-trench-transform triple junction. *Geology*, 36(11), 895–898. <https://doi.org/10.1130/g25356a>
- Audet, P., Schutt, D. L., Schaeffer, A. J., Estève, C., Aster, R. C., & Cubley, J. F. (2020). Moho variations across the northern Canadian cordillera. *Seismological Research Letters*, 91(6), 3076–3085. <https://doi.org/10.1785/0220200166>
- Audet, P., Sole, C., & Schaeffer, A. J. (2016). Control of lithospheric inheritance on neotectonic activity in northwestern Canada? *Geology*, 44(10), 807–810. <https://doi.org/10.1130/g38118.1>
- Aulbach, S., Griffin, W. L., Pearson, N. J., & O'Reilly, S. Y. (2013). Nature and timing of metasomatism in the stratified mantle lithosphere beneath the central Slave craton (Canada). *Chemical Geology*, 352, 153–169. <https://doi.org/10.1016/j.chemgeo.2013.05.037>
- Aulbach, S., Pearson, N. J., O'Reilly, S. Y., & Doyle, B. J. (2007). Origins of xenolithic eclogites and pyroxenites from the central slave craton, Canada. *Journal of Petrology*, 48(10), 1843–1873. <https://doi.org/10.1093/petrology/egm041>
- Babaie Mahani, A., Esfahani, F., Kao, H., Gaucher, M., Hayes, M., Visser, R., & Venables, S. (2019). A systematic study of earthquake source mechanism and regional stress field in the southern Montney unconventional play of northeast British Columbia, Canada. *Seismological Research Letters*, 91(1), 195–206. <https://doi.org/10.1785/0220190230>
- Baker, M. G., Heath, D. C., Schutt, D. L., Aster, R. C., Cubley, J. F., & Freymueller, J. T. (2020). The Mackenzie mountains Earthscope project: Studying active deformation in the northern North American Cordillera from Margin to Craton. *Seismological Research Letters*, 91(1), 521–532. <https://doi.org/10.1785/0220190139>
- Bank, C.-G., Bostock, M. G., Ellis, R. M., & Cassidy, J. F. (2000). A reconnaissance teleseismic study of the upper mantle and transition zone beneath the Archean Slave craton in NW Canada. *Tectonophysics*, 319(3), 151–166. [https://doi.org/10.1016/s0040-1951\(00\)00034-2](https://doi.org/10.1016/s0040-1951(00)00034-2)
- Bao, X., Eaton, D. W., & Guest, B. (2014). Plateau uplift in Western Canada caused by lithospheric delamination along a craton edge. *Nature Geoscience*, 7(11), 830–833. <https://doi.org/10.1038/ngeo2270>
- Barchek, G., Abers, G. A., Adams, A. N., Bécel, A., Collins, J., Gaherty, J. B., et al. (2020). The Alaska amphibious community seismic experiment. *Seismological Research Letters*, 91(6), 3054–3063. <https://doi.org/10.1785/0220200189>
- Bastow, I. D., Eaton, D. W., Kendall, J., Helffrich, G., Snyder, D. B., Thompson, D. A., et al. (2015). The Hudson Bay lithospheric experiment (HuBLE): Insights into Precambrian plate tectonics and the development of mantle keels. *Geological Society London Special Publications*, 389(1), 41–67. <https://doi.org/10.1144/SP389.7>
- Beck, M., & Noson, L. (1972). Anomalous palaeolatitudes in cretaceous granitic rocks. *Nature; Physical Science*, 235(53), 11–13. <https://doi.org/10.1038/physci235011a0>
- Bedle, H., & Van der Lee, S. (2009). S velocity variations beneath North America. *Journal of Geophysical Research*, 114(B7), 22. <https://doi.org/10.1029/2008jb005949>
- Bent, A. L., Côté, T. J., Seywerd, H. C. J., McCormack, D. A., & Coyle, K. A. (2019). The Canadian national seismograph network: Upgrade and status. *Seismological Research Letters*, 91(2A), 585–592. <https://doi.org/10.1785/0220190202>
- Berger, A. L., Gulick, S. P. S., Spotila, J. A., Upton, P., Jaeger, J. M., Chapman, J. B., et al. (2008). Quaternary tectonic response to intensified glacial erosion in an orogenic wedge. *Nature Geoscience*, 1(11), 793–799. <https://doi.org/10.1038/geo0334>
- Berman, R., Davis, W., & Pehrsson, S. (2007). Collisional Snowbird tectonic zone resurrected: Growth of Laurentia during the 1.9 Ga accretionary phase of the Hudsonian orogeny. *Geology*, 35(10), 911–914. <https://doi.org/10.1130/G23771A.1>
- Boogs, K. J. E., Aster, R. C., Audet, P., Brunet, G., Clowes, R. M., De Groot-Hedlin, C. D., et al. (2018). EON-ROSE and the Canadian cordillera array – Building bridges to span Earth system science in Canada. *Geoscience Canada*, 45(2), 97–109. <https://doi.org/10.12789/geocanj.2018.45.136>
- Bostock, M. (1998). Mantle stratigraphy and evolution of the Slave province. *Journal of Geophysical Research*, 103(B9), 21183–21200. <https://doi.org/10.1029/98JB01069>
- Bostock, M. G., & Vandecar, J. C. (1995). Upper mantle structure of the northern Cascadia subduction zone. *Canadian Journal of Earth Sciences*, 32(1), 1–12. <https://doi.org/10.1139/e95-001>
- Boyce, A., Bastow, I. D., Cottaar, S., Kounoudis, R., Guilloud De Courbeville, J., Caunt, E., & Desai, S. (2021). AFRP20: New P-wavespeed model for the African mantle reveals two whole-mantle plumes below East Africa and neoproterozoic modification of the Tanzania Craton. *Geochemistry, Geophysics, Geosystems*, 22(3). <https://doi.org/10.1029/2020GC009302>
- Boyce, A., Bastow, I. D., Darbyshire, F. A., Ellwood, A. G., Gilligan, A., Levin, V., & Menke, W. (2016). Subduction beneath Laurentia modified the eastern North American cratonic edge: Evidence from P wave and S wave tomography. *Journal of Geophysical Research*, 121(7), 5013–5030. <https://doi.org/10.1002/2016JB012838>
- Boyce, A., Bastow, I. D., Golos, E. M., Rondenay, S., Burdick, S., & Van der Hilst, R. D. (2019). Variable modification of continental lithosphere during the proterozoic grenville orogeny: Evidence from teleseismic P-wave tomography. *Earth and Planetary Science Letters*, 525, 115763. <https://doi.org/10.1016/j.epsl.2019.115763>
- Boyce, A., Bastow, I. D., Rondenay, S., & Van der Hilst, R. D. (2017). From relative to absolute teleseismic travel-times: The Absolute Arrival-time Recovery Method (AARM). *Bulletin of Seismological Society of America*, 107(5), 2511–2520. <https://doi.org/10.1785/0120170021>

- Brothers, D. S., Miller, N. C., Barrie, J. V., Haeussler, P. J., Greene, H. G., Andrews, B. D., et al. (2020). Plate boundary localization, slip-rates and rupture segmentation of the Queen Charlotte Fault based on submarine tectonic geomorphology. *Earth and Planetary Science Letters*, 530, 115882. <https://doi.org/10.1016/j.epsl.2019.115882>
- Burdick, S., Van der Hilst, R. D., Vernon, F. L., Martynov, V., Cox, T., Eakins, J., et al. (2014). Model update January 2013: Upper mantle heterogeneity beneath North America from travel-time tomography with global and US array transportable array data. *Seismological Research Letters*, 85(1), 77–81. <https://doi.org/10.1785/0220130098>
- Burdick, S., Vernon, F. L., Martynov, V., Eakins, J., Cox, T., Tytell, J., et al. (2017). Model update May 2016: Upper-mantle heterogeneity beneath North America from travel-time tomography with global and US array data. *Seismological Research Letters*, 88(2A), 319–325. <https://doi.org/10.1785/0220160186>
- Bustin, A. M. M., Hyndman, R. D., Kao, H., & Cassidy, J. F. (2007). Evidence for underthrusting beneath the Queen Charlotte Margin, British Columbia, from teleseismic receiver function analysis. *Geophysical Journal International*, 171(3), 1198–1211. <https://doi.org/10.1111/j.1365-246x.2007.03583.x>
- Calkins, J. A., Zandt, G., Girardi, J., Dueker, K., Gehrels, G. E., & Ducea, M. N. (2010). Characterization of the crust of the Coast Mountains Batholith, British Columbia, from P to S converted seismic waves and petrologic modeling. *Earth and Planetary Science Letters*, 289(1), 145–155. <https://doi.org/10.1016/j.epsl.2009.10.037>
- Calvert, A. J., & Ludden, J. N. (1999). Archean continental assembly in the southeastern superior province of Canada. *Tectonics*, 18(3), 412–429. <https://doi.org/10.1029/1999TC900006>
- Card, K. (1990). A review of the superior province of the Canadian shield, a product of Archean accretion. *Precambrian Research*, 48(1–2), 99–156. [https://doi.org/10.1016/0301-9268\(90\)90059-y](https://doi.org/10.1016/0301-9268(90)90059-y)
- Castaneda, R. A. S., Abers, G. A., Eilon, Z. C., & Christensen, D. H. (2021). Teleseismic attenuation, temperature, and melt of the upper mantle in the Alaska subduction zone. *Journal of Geophysical Research*, 126(7). <https://doi.org/10.1029/2021jb021653>
- Cecile, M. P., Morrow, D. W., & Williams, G. K. (1997). Early paleozoic (Cambrian to early Devonian) tectonic framework, Canadian cordillera. *Bulletin of Canadian Petroleum Geology*, 45(1), 54–74.
- Chen, C.-W., Rondenay, S., Evans, R. L., & Snyder, D. B. (2009). Geophysical detection of relict metasomatism from an Archean (~3.5 Ga) subduction zone. *Science*, 326(5956), 1089–1091. <https://doi.org/10.1126/science.1178477>
- Chen, C.-W., Rondenay, S., Weeraratne, D. S., & Snyder, D. B. (2007). New constraints on the upper mantle structure of the Slave craton from Rayleigh wave inversion. *Geophysical Research Letters*, 34(10), L10301. <https://doi.org/10.1029/2007gl029535>
- Chen, Y., Gu, Y. J., Currie, C. A., Johnston, S. T., Hung, S.-H., Schaeffer, A. J., & Audet, P. (2019). Seismic evidence for a mantle suture and implications for the origin of the Canadian Cordillera. *Nature Communications*, 10(1), 2249. <https://doi.org/10.1038/s41467-019-09804-8>
- Chen, Y., Gu, Y. J., & Hung, S.-H. (2018). A new appraisal of lithospheric structures of the Cordillera-craton boundary region in Western Canada. *Tectonics*, 37(9), 3207–3228. <https://doi.org/10.1029/2018tc004956>
- Christensen, D. H., & Abers, G. A. (2010). Seismic anisotropy under central Alaska from SKS splitting observations. *Journal of Geophysical Research*, 115(B4), B04315. <https://doi.org/10.1029/2009JB006712>
- Clemnott, E. J., Sigloch, K., Mihalynuk, M. G., Seton, M., Henderson, M. A., Hosseini, K., et al. (2020). A quantitative tomotectonic plate reconstruction of Western North America and the Eastern Pacific basin. *Geochemistry, Geophysics, Geosystems*, 21(8). <https://doi.org/10.1029/2020gc009117>
- Clowes, R. M., Hammer, P. T. C., Fernández-Viejo, G., & Welford, J. K. (2005). Lithospheric structure in northwestern Canada from lithoprobe seismic refraction and related studies: A synthesis. *Canadian Journal of Earth Sciences*, 42(6), 1277–1293. <https://doi.org/10.1139/e04-069>
- Cui, L., & Atkinson, G. M. (2016). Spatiotemporal variations in the completeness magnitude of the composite Alberta seismicity catalog (CASC). *Seismological Research Letters*, 87(4), 853–863. <https://doi.org/10.1785/0220150268>
- D'Alessandro, A., & Ruppert, N. A. (2012). Evaluation of location performance and magnitude of completeness of the Alaska regional seismic network by the SNES method. *Bulletin of the Seismological Society of America*, 102(5), 2098–2115. <https://doi.org/10.1785/0120110199>
- Daly, K. A., Abers, G. A., Mann, M. E., Roecker, S., & Christensen, D. H. (2021). Subduction of an oceanic plateau across southcentral Alaska: High-resolution seismicity. *Journal of Geophysical Research*, 126(11). <https://doi.org/10.1029/2021jb022809>
- Darbyshire, F. A., Eaton, D. W., & Bastow, I. D. (2013). Seismic imaging of the lithosphere beneath Hudson Bay: Episodic growth of the Laurentian mantle keel. *Earth and Planetary Science Letters*, 373, 179–193. <https://doi.org/10.1016/j.epsl.2013.05.002>
- DeMets, C., & Dixon, T. H. (1999). New kinematic models for Pacific-North America motion from 3 Ma to present, I: Evidence for steady motion and biases in the NUVEL-1A model. *Geophysical Research Letters*, 26(13), 1921–1924. <https://doi.org/10.1029/1999gl900405>
- Dickinson, W. R. (2004). Evolution of the North American cordillera. *Annual Review of Earth and Planetary Sciences*, 32(1), 13–45. <https://doi.org/10.1146/annurev.earth.32.101802.120257>
- Dixon, J., Stihler, S., Power, J., Haney, M., Parker, T., Searcy, C., & Prejean, S. (2013). Catalog of earthquake hypocenters at Alaskan volcanoes: January 1 through December 31, 2012 [Dataset]. U.S. Geological Survey Data Series, 789, 84. Retrieved from <https://pubs.usgs.gov/gds/789/>
- Domeier, M., Shephard, G. E., Jakob, J., Gaina, C., Doubrovine, P. V., & Torsvik, T. H. (2017). Intraoceanic subduction spanned the Pacific in the late cretaceous–paleocene. *Science Advances*, 3(11). <https://doi.org/10.1126/sciadv.aao2303>
- Dueker, K., & Zandt, G. (2005). Magma accretion and the formation of batholiths [Dataset] (Seismic Network). International Federation of Digital Seismograph Networks. [https://doi.org/10.7914/SN/XY\\_2005](https://doi.org/10.7914/SN/XY_2005). Retrieved from [https://www.fdsn.org/networks/detail/XY\\_2005/](https://www.fdsn.org/networks/detail/XY_2005/)
- Eaton, D., Frederiksen, A., & Miong, S. (2004). Shear-wave splitting observations in the lower Great Lakes region: Evidence for regional anisotropic domains and keel-modified asthenospheric flow. *Geophysical Research Letters*, 31(7), 4. <https://doi.org/10.1029/2004GL019438>
- Eberhart-Phillips, D., Christensen, D. H., Brocher, T. M., Hansen, R., Ruppert, N. A., Haeussler, P. J., & Abers, G. A. (2006). Imaging the transition from Aleutian subduction to Yakutat collision in central Alaska, with local earthquakes and active source data. *Journal of Geophysical Research*, 111(B11). <https://doi.org/10.1029/2005jb004240>
- Eeken, T., Goes, S., Pedersen, H. A., Arndt, N. T., & Bouilhol, P. (2018). Seismic evidence for depth-dependent metasomatism in cratons. *Earth and Planetary Science Letters*, 491, 148–159. <https://doi.org/10.1016/j.epsl.2018.03.018>
- Engdahl, E. R., Van der Hilst, R. D., & Buland, R. (1998). Global teleseismic earthquake relocation with improved travel times and procedures for depth determination. *Bulletin of the Seismological Society of America*, 88(3), 722–743. <https://doi.org/10.1785/bssa0880030722>
- Engebretson, D. C., Cox, A., & Gordon, R. G. (1984). Relative motions between oceanic plates of the Pacific Basin. *Journal of Geophysical Research*, 89(B12), 10291–10310. <https://doi.org/10.1029/jb089ib12p10291>
- Engebretson, D. C., Cox, A., & Gordon, R. G. (1985). Relative motions between oceanic and continental plates in the Pacific Basin. *Geological Society of America Special Papers*, (60), 206–260. <https://doi.org/10.1130/SPE206-p1>
- Estève, C., Audet, P., Schaeffer, A. J., Schutt, D. L., Aster, R. C., & Cubley, J. (2020). The upper mantle structure of Northwestern Canada from teleseismic body wave tomography. *Journal of Geophysical Research*, 125(2). <https://doi.org/10.1029/2019jb018837>

- Estève, C., Schaeffer, A. J., & Audet, P. (2019). Upper mantle structure underlying the diamondiferous Slave craton from teleseismic body-wave tomography. *Tectonophysics*, 757, 187–202. <https://doi.org/10.1016/j.tecto.2019.01.012>
- Frederiksen, A. W., Bollmann, T., Darbyshire, F. A., & Van der Lee, S. (2013). Modification of continental lithosphere by tectonic processes: A tomographic image of central North America. *Journal of Geophysical Research*, 118(3), 1051–1066. <https://doi.org/10.1002/jgrb.50060>
- Frederiksen, A. W., Bostock, M. G., & Cassidy, J. F. (2001). S-wave velocity structure of the Canadian upper mantle. *Physics of the Earth and Planetary Interiors*, 124(3), 175–191. [https://doi.org/10.1016/S0031-9201\(01\)00194-7](https://doi.org/10.1016/S0031-9201(01)00194-7)
- Frederiksen, A. W., Bostock, M. G., VanDecar, J. C., & Cassidy, J. F. (1998). Seismic structure of the upper mantle beneath the northern Canadian Cordillera from teleseismic travel-time inversion. *Tectonophysics*, 294(1–2), 43–55. [https://doi.org/10.1016/s0040-1951\(98\)00095-x](https://doi.org/10.1016/s0040-1951(98)00095-x)
- Fuston, S., & Wu, J. (2021). Raising the Resurrection plate from an unfolded-slab plate tectonic reconstruction of northwestern North America since early Cenozoic time. *GSA Bulletin*, 133(5–6), 1128–1140. <https://doi.org/10.1130/b35677.1>
- Gaherty, J., & Revenaugh, J. (2003). Collaborative research: Canadian northwest seismic experiment [Dataset] (seismic network). International Federation of Digital Seismograph Networks. [https://doi.org/10.7914/SN/XN\\_2003](https://doi.org/10.7914/SN/XN_2003). Retrieved from [https://www.fdsn.org/networks/detail/XN\\_2003/](https://www.fdsn.org/networks/detail/XN_2003/)
- Geological Survey of Canada. (2000). Portable observatories for lithospheric analysis and research investigating seismicity (POLARIS) [Dataset] (Seismic Network). International Federation of Digital Seismograph Networks Retrieved from <http://www.polarisnet.ca/network/polaris-network-locations.html>
- Gosselin, J. M., Cassidy, J. F., & Dosso, S. E. (2015). Shear-wave velocity structure in the vicinity of the 2012 Mw 7.8 Haida Gwaii earthquake from receiver function inversionshear-wave velocity structure in the vicinity of the 2012 Mw 7.8 Haida Gwaii earthquake from RF inversion. *Bulletin of the Seismological Society of America*, 105(2B), 1106–1113. <https://doi.org/10.1785/0120140171>
- Gou, T., Zhao, D., Huang, Z., & Wang, L. (2019). Aseismic deep slab and mantle flow beneath Alaska: Insight from anisotropic tomography. *Journal of Geophysical Research*, 124(2), 1700–1724. <https://doi.org/10.1029/2018jb016639>
- Grand, S. P. (1987). Tomographic inversion for shear velocity beneath the North American plate. *Journal of Geophysical Research*, 92(B13), 14065–14090. <https://doi.org/10.1029/JB092iB13p14065>
- Griffin, W. L., O'Reilly, S. Y., Abe, N., Aulbach, S., Davies, R. M., Pearson, N. J., et al. (2003). The origin and evolution of Archean lithospheric mantle. *Precambrian Research*, 127(1–3), 19–41. [https://doi.org/10.1016/S0301-9268\(03\)00180-3](https://doi.org/10.1016/S0301-9268(03)00180-3)
- Griffin, W. L., O'Reilly, S. Y., Doyle, B. J., Pearson, N. J., Coopersmith, H., Kivi, K., et al. (2004). Lithosphere mapping beneath the North American plate. *Lithos*, 77(1), 873–922. <https://doi.org/10.1016/j.lithos.2004.03.034>
- Gu, Y. J., Okeler, A., Shen, L., & Contenti, S. (2011). The Canadian Rockies and Alberta network (CRANE): New constraints on the Rockies and Western Canada sedimentary basin. *Seismological Research Letters*, 82(4), 575–588. <https://doi.org/10.1785/gssr.82.4.575>
- Hanmer, S., Bowring, S., Van Breemen, O., & Parrish, R. (1992). Great Slave Lake shear zone, NW Canada: Mylonitic record of early proterozoic continental convergence, collision and indentation. *Journal of Structural Geology*, 14(7), 757–773. [https://doi.org/10.1016/0191-8141\(92\)90039-y](https://doi.org/10.1016/0191-8141(92)90039-y)
- Hansen, R., & Pavlis, G. (2005). Collaborative research: St. Elias erosion/tectonics project [Dataset] (Seismic Network). International Federation of Digital Seismograph Networks. [https://doi.org/10.7914/SN/XZ\\_2005](https://doi.org/10.7914/SN/XZ_2005) Retrieved from [https://www.fdsn.org/networks/detail/XZ\\_2005/](https://www.fdsn.org/networks/detail/XZ_2005/)
- Hatcher, R. D. (2005). Southern and central Appalachians. *Encyclopedia of Geology*, 72–81. <https://doi.org/10.1016/b0-12-369396-9/00408-1>
- Hatcher, R. D. (2010). The Appalachian orogen: A brief summary. In R. Tollo, M. Bartholomew, J. Hibbard, & P. Karabinos (Eds.), *From Rodinia to Pangea: The lithotectonic record of the appalachian region* (Vol. 206, pp. 1–19). Geological Society of America. [https://doi.org/10.1130/2010.1206\(01\)](https://doi.org/10.1130/2010.1206(01))
- Hayward, N. (2015). Geophysical investigation and reconstruction of lithospheric structure and its control on geology, structure, and mineralization in the cordillera of northern Canada and eastern Alaska. *Tectonics*, 34(10), 2165–2189. <https://doi.org/10.1002/2015tc003871>
- Hayward, N., & Paradis, S. (2021). Geophysical reassessment of the role of ancient lineaments on the development of the Western Laurentian margin and its sediment-hosted Zn–Pb deposits, Yukon and Northwest Territories, Canada. *Canadian Journal of Earth Sciences*, 58(12), 1283–1300. <https://doi.org/10.1139/cjes-2021-0003>
- Heaman, L. M., & Kjarsgaard, B. A. (2000). Timing of eastern North American kimberlite magmatism: Continental extension of the great meteor hotspot track? *Earth and Planetary Science Letters*, 178(3), 253–268. [https://doi.org/10.1016/S0012-821X\(00\)00079-0](https://doi.org/10.1016/S0012-821X(00)00079-0)
- Heaman, L. M., & Pearson, D. G. (2010). Nature and evolution of the Slave Province subcontinental lithospheric mantle. *Canadian Journal of Earth Sciences*, 47(4), 369–388. <https://doi.org/10.1139/e09-046>
- Hoffman, P. F. (1987). Continental transform tectonics: Great Slave Lake shear zone (ca. 1.9 Ga), northwest Canada. *Geology*, 15(9), 785–788. [https://doi.org/10.1130/0091-7613\(1987\)15<785:cttgs>2.0.co;2](https://doi.org/10.1130/0091-7613(1987)15<785:cttgs>2.0.co;2)
- Hoffman, P. F. (1988). United plates of America, the birth of a craton - early proterozoic assembly and growth of Laurentia. *Annual Review of Earth and Planetary Sciences*, 16(1), 543–603. <https://doi.org/10.1146/annurev.ea.16.050188.002551>
- Hosseini, K., & Sigloch, K. (2017). ObspyDMT: A Python toolbox for retrieving and processing large seismological datasets. *Solid Earth*, 8(5), 1047–1070. <https://doi.org/10.5194/se-8-1047-2017>
- Hosseini, K., Sigloch, K., Tsekhmistrovskiy, M., Zaheri, A., Nissen-Meyer, T., & Igel, H. (2019). Global mantle structure from multifrequency tomography using P, PP and P-diffracted waves. *Geophysical Journal International*, 220(1), 96–141. <https://doi.org/10.1093/gji/ggz394>
- Hyndman, R. D. (2015). Tectonics and Structure of the Queen Charlotte fault zone, Haida Gwaii, and large thrust earthquakes: Tectonics and structure of the QCF zone and large thrust earthquakes. *Bulletin of the Seismological Society of America*, 105(2B), 1058–1075. <https://doi.org/10.1785/0120140181>
- Hynes, A., & Rivers, T. (2010). Protracted continental collision - evidence from the Grenville orogen. *Canadian Journal of Earth Sciences*, 47(5), 591–620. <https://doi.org/10.1139/E10-003>
- Indiana University Bloomington (IU Bloomington). (1998). PEPP-Indiana [Dataset] (Seismic Network). International Federation of Digital Seismograph Networks. Retrieved from <https://www.fdsn.org/networks/detail/PN/>
- IRIS OBSIP. (2011). Cascadia initiative community experiment - OBS component [Dataset] (Seismic Network). International Federation of Digital Seismograph Networks. [https://doi.org/10.7914/SN/7D\\_2011](https://doi.org/10.7914/SN/7D_2011)
- Jadamec, M. A., & Billen, M. I. (2010). Reconciling surface plate motions with rapid three-dimensional mantle flow around a slab edge. *Nature*, 465(7296), 338–341. <https://doi.org/10.1038/nature09053>
- Jiang, C., Schmandt, B., Ward, K. M., Lin, F., & Worthington, L. L. (2018). Upper mantle seismic structure of Alaska from Rayleigh and S wave tomography. *Geophysical Research Letters*, 45(19), 10350–10359. <https://doi.org/10.1029/2018gl079406>
- Johnston, S. T. (2001). The great Alaskan terrane wreck: Reconciliation of paleomagnetic and geological data in the northern cordillera. *Earth and Planetary Science Letters*, 193(3–4), 259–272. [https://doi.org/10.1016/s0012-821x\(01\)00516-7](https://doi.org/10.1016/s0012-821x(01)00516-7)
- Johnston, S. T. (2008). The cordilleran ribbon continent of North America. *Annual Review of Earth and Planetary Sciences*, 36(1), 495–530. <https://doi.org/10.1146/annurev.earth.36.031207.124331>

- Káráson, H., & Van der Hilst, R. D. (2001). Tomographic imaging of the lowermost mantle with differential times of refracted and diffracted core phases (PKP, P diff). *Journal of Geophysical Research*, 106(B4), 6569–6587. <https://doi.org/10.1029/2000jb900380>
- Kelemen, P. B., Hart, S. R., & Bernstein, S. (1998). Silica enrichment in the continental upper mantle via melt/rock reaction. *Earth and Planetary Science Letters*, 164(1–2), 387–406. [https://doi.org/10.1016/S0012-821X\(98\)00233-7](https://doi.org/10.1016/S0012-821X(98)00233-7)
- Kennett, B. L. N., Engdahl, E. R., & Buland, R. (1995). Constraints on seismic velocities in the Earth from traveltimes. *Geophysical Journal International*, 122(1), 108–124. <https://doi.org/10.1111/j.1365-246X.1995.tb03540.x>
- Kennett, B. L. N., & Gudmundsson, O. (1996). Ellipticity corrections for seismic phases. *Geophysical Journal International*, 127(1), 40–48. <https://doi.org/10.1111/j.1365-246X.1996.tb01533.x>
- Keranen, K. (2011). Broadband recording at the site of great earthquake rupture in the Alaska Megathrust [Dataset] (Seismic Network). International Federation of Digital Seismograph Networks. Retrieved from [https://www.fdsn.org/networks/detail/XM\\_2011/](https://www.fdsn.org/networks/detail/XM_2011/) [https://doi.org/10.7914/SN/XM\\_2011](https://doi.org/10.7914/SN/XM_2011)
- Larsen, C., & Truffer, M. (2007). Glacier seismicity and high resolution motion records: Relation to glacier erosion [Dataset] (Seismic Network). International Federation of Digital Seismograph Networks. Retrieved from [https://www.fdsn.org/networks/detail/XV\\_2007/](https://www.fdsn.org/networks/detail/XV_2007/) [https://doi.org/10.7914/SN/XV\\_2007](https://doi.org/10.7914/SN/XV_2007)
- Laske, G., Masters, G., Ma, Z., & Pasyanos, M. E. (2013). Update on CRUST1.0 - a 1-degree global model of Earth's crust. *Geophysics Research Abstracts*, 15, abstract egu2013-2658 (p. EGU2013-2658).
- Lay, T., Ye, L., Kanamori, H., Yamazaki, Y., Cheung, K. F., Kwong, K., & Koper, K. D. (2013). The October 28, 2012 M w 7.8 Haida Gwaii underthrusting earthquake and tsunami: Slip partitioning along the Queen Charlotte Fault transpressional plate boundary. *Earth and Planetary Science Letters*, 375, 57–70. <https://doi.org/10.1016/j.epsl.2013.05.005>
- Li, C., Van der Hilst, R. D., Engdahl, R., & Burdick, S. (2008). A new global model for P wave speed variations in Earth's mantle. *Geochemistry, Geophysics, Geosystems*, 9(5), a–n. <https://doi.org/10.1029/2007GC001806>
- Li, Z. X., Bogdanova, S. V., Collins, A. S., Davidson, A., Waele, B. D., Ernst, R. E., et al. (2008). Assembly, configuration, and break-up history of Rodinia: A synthesis. *Precambrian Research*, 160(1–2), 179–210. <https://doi.org/10.1016/j.precamres.2007.04.021>
- Liddell, M. V., Bastow, I. D., Rawlinson, N., Darbyshire, F. A., Gilligan, A., & Watson, E. (2018). Precambrian plate tectonics in Northern Hudson Bay: Evidence from P and S-wave seismic tomography and analysis of source side effects in relative arrival-time datasets. *Journal of Geophysical Research*, 123(7), 5690–5709. <https://doi.org/10.1029/2018jb015473>
- Lister, G. S., Etheridge, M. A., & Symonds, P. A. (1986). Detachment faulting and the evolution of passive continental margins. *Geology*, 14(3), 246–250. [https://doi.org/10.1130/0091-7613\(1986\)14<246:dfateo>2.0.co;2](https://doi.org/10.1130/0091-7613(1986)14<246:dfateo>2.0.co;2)
- Liu, J., Pearson, D. G., Wang, L. H., Mather, K. A., Kjarsgaard, B. A., Schaeffer, A. J., et al. (2021). Plume-driven reactivation of deep continental lithospheric mantle. *Nature*, 592(7856), 732–736. <https://doi.org/10.1038/s41586-021-03395-5>
- Lund, K. (2008). Geometry of the neoproterozoic and paleozoic rift margin of Western Laurentia: Implications for mineral deposit settings. *Geosphere*, 4(2), 429–444. <https://doi.org/10.1130/ges00121.1>
- Mann, M. E., Abers, G. A., Daly, K. A., & Christensen, D. H. (2022). Subduction of an oceanic plateau across southcentral Alaska: Scattered-wave imaging. *Journal of Geophysical Research*, 127(1). <https://doi.org/10.1029/2021jb022697>
- Martin-Short, R., Allen, R., Bastow, I. D., Porritt, R. W., & Miller, M. S. (2018). Seismic imaging of the Alaska subduction zone: Implications for slab geometry and volcanism. *Geochemistry, Geophysics, Geosystems*, 19(11), 4541–4560. <https://doi.org/10.1029/2018gc007962>
- Martin-Short, R., Allen, R. M., & Bastow, I. D. (2016). Subduction geometry beneath south central Alaska and its relationship to volcanism. *Geophysical Research Letters*, 43(18), 9509–9517. <https://doi.org/10.1002/2016gl070580>
- Mazzotti, S., Dragert, H., Henton, J., Schmidt, M., Hyndman, R., James, T., & Craymer, M. (2003). Current tectonics of northern Cascadia from a decade of GPS measurements. *Journal of Geophysical Research*, 108(B12), 2554. <https://doi.org/10.1029/2003jb002653>
- McGill University (Canada). (2017). McGill Dawson-septimus induced seismicity study [Dataset] (Seismic Network). International Federation of Digital Seismograph Networks. Retrieved from [https://www.fdsn.org/networks/detail/XL\\_2017/](https://www.fdsn.org/networks/detail/XL_2017/)
- McPherson, A. M., Christensen, D. H., Abers, G. A., & Tape, C. (2020). Shear wave splitting and mantle flow beneath Alaska. *Journal of Geophysical Research*, 125(4). <https://doi.org/10.1029/2019JB018329>
- Mercier, J.-P., Bostock, M. G., Cassidy, J. F., Dueker, K., Gaherty, J. B., Garner, E. J., et al. (2009). Body-wave tomography of Western Canada. *Tectonophysics*, 475(3–4), 480–492. <https://doi.org/10.1016/j.tecto.2009.05.030>
- Monger, J. W. H. (1997). Plate tectonics and Northern Cordilleran geology: An unfinished revolution. *Geoscience Canada*, 24(4).
- Montelli, R., Nolet, G., Dahlen, F., & Masters, G. (2006). A catalogue of deep mantle plumes: New results from finite-frequency tomography. *Geochemistry, Geophysics, Geosystems*, 7(11), Q11007. <https://doi.org/10.1029/2006GC001248>
- Müller, R. D., Cannon, J., Qin, X., Watson, R. J., Gurnis, M., Williams, S., et al. (2018). GPlates: Building a virtual Earth through deep time. *Geochemistry, Geophysics, Geosystems*, 19(7), 2243–2261. <https://doi.org/10.1029/2018gc007584>
- Müller, R. D., Zahirovic, S., Williams, S. E., Cannon, J., Seton, M., Bower, D. J., et al. (2019). A global plate model including lithospheric deformation along major rifts and orogens since the triassic. *Tectonics*, 38(6), 1884–1907. <https://doi.org/10.1029/2018tc005462>
- Nabelek, J., & Braunmiller, J. (2012). Plate boundary evolution and physics at an oceanic transform fault system [Dataset] (Seismic Network). International Federation of Digital Seismograph Networks. [https://doi.org/10.7914/SN/X9\\_2012](https://doi.org/10.7914/SN/X9_2012)
- Nabelek, J., & Braunmiller, J. (2013). Seismicity, structure and dynamics of the Gorda deformation zone [Dataset] (Seismic Network). International Federation of Digital Seismograph Networks. [https://doi.org/10.7914/SN/ZS\\_2013](https://doi.org/10.7914/SN/ZS_2013)
- Natural Resources Canada (NRCCAN Canada). (1975). Canadian national seismograph network [Dataset] (Seismic Network). International Federation of Digital Seismograph Networks. Retrieved from <https://doi.org/10.7914/SN/CN> <https://www.fdsn.org/networks/detail/CN/>
- Natural Resources Canada (NRCCAN Canada). (2002). Canadian seismic research network [Dataset] (Seismic Network). International Federation of Digital Seismograph Networks. Retrieved from <http://www.earthquakescanada.nrcan.gc.ca/stndon/>
- Natural Resources Canada (NRCCAN Canada). (2018). GSC-BCOGC induced seismicity study [Dataset] (Seismic Network). International Federation of Digital Seismograph Networks. Retrieved from [https://www.fdsn.org/networks/detail/1E\\_2018/](https://www.fdsn.org/networks/detail/1E_2018/)
- Nayak, A., Eberhart-Phillips, D., Ruppert, N. A., Fang, H., Moore, M. M., Tape, C., et al. (2020). 3D seismic velocity models for Alaska from joint tomographic inversion of body-wave and surface-wave data. *Seismological Research Letters*, 91(6), 3106–3119. <https://doi.org/10.1785/0220200214>
- Nettles, M., & Dziewonski, A. (2008). Radially anisotropic shear velocity structure of the upper mantle globally and beneath North America. *Journal of Geophysical Research*, 113(B2), B02303. <https://doi.org/10.1029/2006JB004819>
- NOAA National Oceanic and Atmospheric Administration (USA). (1967). National tsunami warning center Alaska seismic network [Dataset] (Seismic Network). International Federation of Digital Seismograph Networks. Retrieved from <https://www.fdsn.org/networks/detail/AT/> <https://doi.org/10.7914/SN/AT>

- Nolet, G. (1987). Seismic wave propagation and seismic tomography. In G. Nolet (Ed.), *Seismic tomography: With applications in global seismology and exploration geophysics, 1–23* (pp. 1–23). Springer Netherlands. [https://doi.org/10.1007/978-94-009-3899-1\\_1](https://doi.org/10.1007/978-94-009-3899-1_1)
- North, R. G. (1994). The Canadian nation seismograph network. *Annales de Geophysicae*, 37(5), 1045–1048.
- Oppenheimer, D. H., Bittenbinder, A. N., Bogaert, B. M., Buland, R. P., Dietz, L. D., Hansen, R. A., et al. (2005). The seismic project of the national tsunami hazard mitigation program. *Natural Hazards*, 35(1), 59–72. <https://doi.org/10.1007/s11069-004-2404-2>
- Page, R. A., Biswas, N. N., Lahr, J. C., & Pulpun, H. (1991). Seismicity of continental Alaska. In *Neotectonics of North North America* (pp. 47–68). Geological Society of America. <https://doi.org/10.1130/DNAG-CSMS-NEO.47>
- Pearson, D. G., & Wittig, N. (2008). Formation of Archaean continental lithosphere and its diamonds: The root of the problem. *Journal of Geological Society London*, 165(5), 895–914. <https://doi.org/10.1144/0016-76492008-003>
- Priestley, K., McKenzie, D., & Ho, T. (2019). A lithosphere - Asthenosphere boundary - a global model derived from multimode surface-wave tomography and petrology. In H. Yuan & B. Romanowicz (Eds.), *Lithospheric discontinuities. Geophysical monograph* (1st ed., Vols, Vol. 239, pp. 111–123). American Geophysical Union and John Wiley & Sons, Inc. <https://doi.org/10.1002/9781119249740>
- Qi, C., Zhao, D., & Chen, Y. (2007). Search for deep slab segments under Alaska. *Physics of the Earth and Planetary Interiors*, 165(1–2), 68–82. <https://doi.org/10.1016/j.pepi.2007.08.004>
- Ratchkovski, N. A., & Hansen, R. A. (2002). New evidence for segmentation of the Alaska subduction zone. *Bulletin of the Seismological Society of America*, 92(5), 1754–1765. <https://doi.org/10.1785/0120000269>
- Rawlinson, N., & Kennett, B. (2004). Rapid estimation of relative and absolute delay times across a network by adaptive stacking. *Geophysical Journal International*, 157(1), 332–340. <https://doi.org/10.1111/j.1365-246X.2004.02188.x>
- Rawlinson, N., & Spakman, W. (2016). On the use of sensitivity tests in seismic tomography. *Geophysical Journal International*, 205(2), 1221–1243. <https://doi.org/10.1093/gji/ggw084>
- Ringler, A. T., Anthony, R. E., Wilson, D. C., Auerbach, D., Bargabus, S., Davis, P., et al. (2021). A review of timing accuracy across the global seismographic network. *Seismological Research Letters*, 92(4), 2270–2281. <https://doi.org/10.1785/0220200394>
- Ritsema, J., Deuss, A., Van Heijst, H.-J., & Woodhouse, J. (2011). S40RTS: A degree-40 shear-velocity model for the mantle from new Rayleigh wave dispersion, teleseismic traveltime and normal-mode splitting function measurements. *Geophysical Journal International*, 184(3), 1223–1236. <https://doi.org/10.1111/j.1365-246X.2010.04884.x>
- Rivers, T. (2009). The Grenville Province as a large hot long-duration collisional orogen – Insights from the spatial and thermal evolution of its orogenic fronts. *Geological Society London Special Publications*, 327(1), 405–444. <https://doi.org/10.1144/SP327.17>
- Rohr, K. M. M., Scheidhauer, M., & Trebu, A. M. (2000). Transpression between two warm mafic plates: The Queen Charlotte fault revisited. *Journal of Geophysical Research*, 105(B4), 8147–8172. <https://doi.org/10.1029/1999jb000403>
- Roth, M. P., Verdecchia, A., Harrington, R. M., & Liu, Y. (2020). High-resolution imaging of hydraulic-fracturing-induced earthquake clusters in the Dawson-septimus area, Northeast British Columbia, Canada. *Seismological Research Letters*, 91(5), 2744–2756. <https://doi.org/10.1785/0220200086>
- Rutgers University (2013). Ocean observatories initiative [Dataset]. International Federation of Digital Seismograph Networks. (Seismic Network). <https://doi.org/10.7914/SN/OO>
- Saltus, R. W., & Hudson, T. L. (2007). Regional magnetic anomalies, crustal strength, and the location of the northern Cordilleran fold-and-thrust belt. *Geology*, 35(6), 567–570. <https://doi.org/10.1130/g23470a.1>
- Savard, G., Bostock, M. G., Hutchinson, J., Kao, H., Christensen, N. I., & Peacock, S. M. (2020). The northern terminus of Cascadia subduction. *Journal of Geophysical Research*, 125(6). <https://doi.org/10.1029/2019jb018453>
- Schaeffer, A., & Lebedev, S. (2014). Imaging the North American continent using waveform inversion of global and USAArray data. *Earth and Planetary Science Letters*, 402, 26–41. <https://doi.org/10.1016/j.epsl.2014.05.014>
- Schmandt, B., & Lin, F. (2014). P and S wave tomography of the mantle beneath the United States. *Geophysical Research Letters*, 41(18), 6342–6349. <https://doi.org/10.1002/2014GL061231>
- Schmidberger, S. S., Simonetti, A., Heaman, L. M., Creaser, R. A., & Whiteford, S. (2007). Lu–Hf, in-situ Sr and Pb isotope and trace element systematics for mantle eclogites from the Diavik diamond mine: Evidence for Paleoproterozoic subduction beneath the Slave craton, Canada. *Earth and Planetary Science Letters*, 254(1–2), 55–68. <https://doi.org/10.1016/j.epsl.2006.11.020>
- Schultz, R., Stern, V., Gu, Y. J., & Eaton, D. (2015). Detection threshold and location resolution of the Alberta geological Survey earthquake catalogue. *Seismological Research Letters*, 86(2A), 385–397. <https://doi.org/10.1785/0220140203>
- Schultz, R., Stern, V., & Yusibayov, J. (2014). Scientific induced seismicity monitoring network [Dataset] (Seismic Network). International Federation of Digital Seismograph Networks. Retrieved from [https://www.fdsn.org/networks/detail/2K\\_2014/](https://www.fdsn.org/networks/detail/2K_2014/) [https://doi.org/10.7914/SN/2K\\_2014](https://doi.org/10.7914/SN/2K_2014)
- Schultz, R., Yusibayov, J., & Shipman, T. (2020). The scientific induced seismicity monitoring network SCISMN Dataset (seismic network). *Alberta Energy Regulator/Alberta Geological Survey AER/AGS Open File Report 2019-09, 10 p*
- Schutt, D. L., & Aster, R. C. (2015). The Mackenzie mountains transect: Active deformation from margin to craton [Dataset] (seismic network). International Federation of Digital Seismograph Networks. [https://doi.org/10.7914/SN/7C\\_2015](https://doi.org/10.7914/SN/7C_2015)
- Schutt, D. L., & Lesher, C. E. (2006). Effects of melt depletion on the density and seismic velocity of garnet and spinel lherzolite. *Journal of Geophysical Research*, 111(B5), a–n. <https://doi.org/10.1029/2003JB002950>
- Schutt, D. L., & Lesher, C. E. (2010). Compositional trends among kaapvaal craton garnet peridotite xenoliths and their effects on seismic velocity and density. *Earth and Planetary Science Letters*, 300(3–4), 367–373. <https://doi.org/10.1016/j.epsl.2010.10.018>
- Schutt, D. L., Porritt, R. W., Estève, C., Audet, P., Gosselin, J. M., Schaeffer, A. J., et al. (2023). Lithospheric S wave velocity variations beneath the Mackenzie Mountains and Northern Canadian cordillera. *Journal of Geophysical Research*, 128(1), e2022JB025517. <https://doi.org/10.1029/2022JB025517>
- Scripps Institution of Oceanography. (1986). Global seismograph network - IRIS/IDA [Dataset] (Seismic Network). International Federation of Digital Seismograph Networks. <https://doi.org/10.7914/SN/II>. Retrieved from <https://www.fdsn.org/networks/detail/II>
- Sigloch, K. (2011). Mantle provinces under North America from multifrequency P wave tomography. *Geochemistry, Geophysics, Geosystems*, 12(2). <https://doi.org/10.1029/2010GC003421>
- Sigloch, K., & Mihalynuk, M. G. (2013). Intra-oceanic subduction shaped the assembly of Cordilleran North America. *Nature*, 496(7443), 50–56. <https://doi.org/10.1038/nature12019>
- Sigloch, K., & Mihalynuk, M. G. (2017). Mantle and geological evidence for a Late Jurassic–Cretaceous suture spanning North America. *GSA Bulletin*, 129(11–12), 1489–1520. <https://doi.org/10.1130/b31529.1>
- Simmons, N. A., Myers, S. C., Johannesson, G., & Matzel, E. (2012). LLNL-G3Dv3: Global P wave tomography model for improved regional and teleseismic travel time prediction. *Journal of Geophysical Research*, 117(B10). <https://doi.org/10.1029/2012JB009525>

- Sleep, N. (1990). Hotspots and mantle plumes: Some phenomenology. *Journal of Geophysical Research*, 95(B5), 6715–6736. <https://doi.org/10.1029/JB095iB05p06715>
- Smith, A. J., Hyndman, R. D., Cassidy, J. F., & Wang, K. (2003). Structure, seismicity, and thermal regime of the Queen Charlotte transform margin. *Journal of Geophysical Research*, 108(B11), 2539. <https://doi.org/10.1029/2002jb002247>
- Snyder, D. B., Bostock, M. G., & Lockhart, G. D. (2003). Two anisotropic layers in the Slave craton. *Lithos*, 71(2), 529–539. <https://doi.org/10.1016/j.lithos.2003.09.001>
- Song, X., & Christensen, D. (2004). Csed: Observational and theoretical constraints on the structure and rotation of the inner core [Dataset] (Seismic Network). International Federation of Digital Seismograph Networks. Retrieved from [https://www.fdsn.org/networks/detail/XR\\_2004/](https://www.fdsn.org/networks/detail/XR_2004/) [https://doi.org/10.7914/SN/XR\\_2004](https://doi.org/10.7914/SN/XR_2004)
- Spakman, W., & Nolet, G. (1988). Imaging algorithms, accuracy and resolution in delay time tomography. In *Mathematical geophysics* (pp. 155–187). Springer. [https://doi.org/10.1007/978-94-009-2857-2\\_8](https://doi.org/10.1007/978-94-009-2857-2_8)
- St-Onge, M., Searle, M., & Wodicka, N. (2006). Trans-Hudson Orogen of North America and Himalaya-Karakoram-Tibetan Orogen of Asia: Structural and thermal characteristics of the lower and upper plates. *Tectonics*, 25(4). <https://doi.org/10.1029/2005TC001907>
- Tange, O. (2020). GNU Parallel is a general parallelizer to run multiple serial command line programs in parallel without changing them. Gnu parallel 20200522 ('kraftwerk'). *Zenodo*. <https://doi.org/10.5281/zenodo.3841377>
- Tape, C., Christensen, D., Moore-Driskell, M. M., Sweet, J., & Smith, K. (2017). Southern Alaska lithosphere and mantle observation network (SALMON): A seismic experiment covering the active arc by road, boat, plane, and helicopter. *Seismological Research Letters*, 88(4), 1185–1202. <https://doi.org/10.1785/0220160229>
- Tape, C., Christensen, D. H., & Moore-Driskell, M. M. (2015). Southern Alaska lithosphere and mantle observation network [Dataset] (Seismic Network). International Federation of Digital Seismograph Networks. Retrieved from [https://www.fdsn.org/networks/detail/ZE\\_2015/](https://www.fdsn.org/networks/detail/ZE_2015/) [https://doi.org/10.7914/SN/ZE\\_2015](https://doi.org/10.7914/SN/ZE_2015)
- Tesuaro, M., Kaban, M. K., Mooney, W. D., & Cloetingh, S. (2014). NACr14: A 3D model for the crustal structure of the North American continent. *Tectonophysics*, 631, 65–86. <https://doi.org/10.1016/j.tecto.2014.04.016>
- Thomas, W. A. (2006). Tectonic inheritance at a continental margin. *Geological Society of America Today*, 16(2), 4–11. [https://doi.org/10.1130/1052-5173\(2006\)016\[4:tiacm\]2.0.co;2](https://doi.org/10.1130/1052-5173(2006)016[4:tiacm]2.0.co;2)
- Tomlinson, E. L., & Kamber, B. S. (2021). Depth-dependent peridotite-melt interaction and the origin of variable silica in the cratonic mantle. *Nature Communications*, 12(1), 1082. <https://doi.org/10.1038/s41467-021-21343-9>
- Toomey, D. R., Allen, R. M., Barclay, A. H., Bell, S. W., Bromirski, P. D., Carlson, R. L., et al. (2014). The Cascadia initiative: A sea change in seismological studies of subduction zones. *Oceanography*, 27(2), 138–150. <https://doi.org/10.5670/oceanog.2014.49>
- TransAlta Corporation. (2013). TransAlta monitoring network [Dataset]. International Federation of Digital Seismograph Networks. Retrieved from <http://www.transalta.com/> (Seismic Network)
- Umhoefer, P. J. (2000). Where are the missing faults in translated terranes? *Tectonophysics*, 326(1–2), 23–35. [https://doi.org/10.1016/s0040-1951\(00\)00144-x](https://doi.org/10.1016/s0040-1951(00)00144-x)
- University of Bristol (Uk). (2007). Hudson Bay lithospheric experiment (HUBLE) [Dataset] (Seismic Network). International Federation of Digital Seismograph Networks. Retrieved from [http://www.fdsn.org/networks/detail/X5\\_2007/](http://www.fdsn.org/networks/detail/X5_2007/)
- University of Calgary (U of C Canada). (2018). EON-ROSE [Dataset] (Seismic Network). International Federation of Digital Seismograph Networks. Retrieved from <https://www.fdsn.org/networks/detail/EO/> <https://doi.org/10.7914/SN/EO>
- University of Alberta (UAlberta Canada). (2006). Canadian rockies and Alberta network (CRANE) [Dataset] (Seismic Network). International Federation of Digital Seismograph Networks. Retrieved from [https://www.fdsn.org/networks/detail/Y5\\_2006/](https://www.fdsn.org/networks/detail/Y5_2006/)
- University of Ottawa (uOttawa Canada). (2013). Yukon-Northwest seismic network [Dataset] (Seismic Network). International Federation of Digital Seismograph Networks. Retrieved from <https://www.fdsn.org/networks/detail/NY/> <https://doi.org/10.7914/SN/NY>
- U.S. Geological Survey. (2016). U.S. Geological Survey networks [Dataset] (seismic network). International Federation of Digital Seismograph Networks. Retrieved from <https://www.fdsn.org/networks/detail/GM/> <https://doi.org/10.7914/SN/GM>
- VanDecar, J., & Crosson, R. (1990). Determination of teleseismic relative phase arrival times using multi-channel cross-correlation and least squares. *Bulletin of the Seismological Society of America*, 80(1), 150–169.
- Van der Lee, S., & Frederiksen, A. W. (2005). Surface Wave tomography applied to the North American upper mantle. *Array Analysis of Broad-band Seismograms*, 157, 67–80. <https://doi.org/10.1029/157GM05>
- Van Staal, C. (2005). The northern appalachians. *Encyclopedia of Geology*, 4, 81–92. <https://doi.org/10.1016/b0-12-369396-9/00407-x>
- Van Stiphout, A. M., Cottaar, S., & Deuss, A. (2019). Receiver function mapping of mantle transition zone discontinuities beneath Alaska using scaled 3-D velocity corrections. *Geophysical Journal International*, 219(2), 1432–1446. <https://doi.org/10.1093/gji/ggz360>
- Various Authors. (1965). International miscellaneous stations (IMS) [Dataset] (Seismic Network). International Federation of Digital Seismograph Networks. Retrieved from <https://www.fdsn.org/networks/detail/IM/>
- Veglio, C., Lawley, C. J. M., Pearson, D. G., Kjarsgaard, B. A., Petts, D. C., & Jackson, S. E. (2022). Olivine xenocrysts reveal carbonated mid-lithosphere in the northern Slave craton. *Lithos*, 414–415, 106633. <https://doi.org/10.1016/j.lithos.2022.106633>
- Venereau, C. M. A., Martin-Short, R., Bastow, I. D., Allen, R. M., & Kounoudis, R. (2019). The role of variable slab dip in driving mantle flow at the eastern edge of the Alaskan subduction margin: Insights from shear-wave splitting. *Geochemistry, Geophysics, Geosystems*, 20(5), 2433–2448. <https://doi.org/10.1029/2018gc008170>
- Villemaire, M., Darbyshire, F. A., & Bastow, I. D. (2012). P-wave tomography of eastern North America: Evidence for mantle evolution from archean to phanerozoic, and modification during subsequent hotspot tectonism. *Journal of Geophysical Research*, 117(B12), a–n. <https://doi.org/10.1029/2012JB009639>
- Wagner, L. S., Anderson, M. L., Jackson, J. M., Beck, S. L., & Zandt, G. (2008). Seismic evidence for orthopyroxene enrichment in the continental lithosphere. *Geology*, 36(12), 935–938. <https://doi.org/10.1130/g25108a.1>
- Waldauser, F., Lippitsch, R., Kissling, E., & Ansorge, J. (2002). High-resolution teleseismic tomography of upper-mantle structure using an *a priori* three-dimensional crustal model. *Geophysical Journal International*, 150(2), 403–414. <https://doi.org/10.1046/j.1365-246x.2002.01690.x>
- Wang, Y., & Tape, C. (2014). Seismic velocity structure and anisotropy of the Alaska subduction zone based on surface wave tomography. *Journal of Geophysical Research*, 119(12), 8845–8865. <https://doi.org/10.1002/2014jb011438>
- Whitmeyer, S. J., & Karlstrom, K. E. (2007). Tectonic model for the Proterozoic growth of North America. *Geosphere*, 3(4), 220–259. <https://doi.org/10.1130/ges00055.1>
- Woods Hole Oceanographic Institution (WHOI). (2010). Cascadia- Keck Dataset. (Seismic Network). International Federation of Digital Seismograph Networks.
- Yang, Y., Gao, S. S., Liu, K. H., Kong, F., & Fu, X. (2021). Mantle flow in the vicinity of the eastern edge of the Pacific-Yukatut Slab: Constraints from shear wave splitting analyses. *Journal of Geophysical Research*, 126(9). <https://doi.org/10.1029/2021jb022354>

- Yorath, C. J., & Hyndman, R. D. (1983). Subsidence and thermal history of queen charlotte basin. *Canadian Journal of Earth Sciences*, 20(1), 135–159. <https://doi.org/10.1139/e83-013>
- Yuan, H., French, S. W., Cupillard, P., & Romanowicz, B. (2014). Lithospheric expression of geological units in central and eastern North America from full waveform tomography. *Earth and Planetary Science Letters*, 402, 176–186. <https://doi.org/10.1016/j.epsl.2013.11.057>
- Yuan, H., Romanowicz, B., Fischer, K. M., & Abt, D. (2011). 3-D shear wave radially and azimuthally anisotropic velocity model of the North American upper mantle. *Geophysical Journal International*, 184(3), 1237–1260. <https://doi.org/10.1111/j.1365-246X.2010.04901.x>
- Yukon Geological Survey. (2016). Yukon Observatory (YO) [Dataset] (Seismic Network). International Federation of Digital Seismograph Networks. Retrieved from [https://www.fdsn.org/networks/detail/YO\\_2016](https://www.fdsn.org/networks/detail/YO_2016)
- Zhao, D., Pirajno, F., Dobretsov, N. L., & Liu, L. (2010). Mantle structure and dynamics under East Russia and adjacent regions. *Russian Geology and Geophysics*, 51(9), 925–938. <https://doi.org/10.1016/j.rgg.2010.08.003>
- Zhao, D., Tian, Y., Lei, J., Liu, L., & Zheng, S. (2009). Seismic image and origin of the Changbai intraplate volcano in East Asia: Role of big mantle wedge above the stagnant Pacific slab. *Physics of the Earth Planetary Interiors*, 173(3–4), 197–206. <https://doi.org/10.1016/j.pepi.2008.11.009>